

Seismic collapse of self-centering steel MRFs with different column base structural properties

Vasileios C. Kamperidis^{a1}, Georgios S. Papavasileiou^b, George S. Kamaris^c and George Vasdravellis^d

^a Department of Civil Engineering and Industrial Design, School of Engineering, Faculty of Science and Engineering, University of Liverpool, The Quadrangle, Brownlow Hill, Liverpool, L69 3GH, UK

^b School of Architecture and Built Environment, University of Wolverhampton, Wolverhampton, WV1 1LY, UK

^c Department of Civil Engineering, Liverpool John Moores University, Liverpool, L3 3AF, UK

^d School of Energy, Geoscience, Infrastructure and Society, Institute for Infrastructure & Environment, Heriot-Watt University, Edinburgh, EH14 4AS, UK

ABSTRACT

The effect of the strength and stiffness characteristics of a previously proposed novel column base on the seismic performance and collapse capacity of steel self-centering moment-resisting frames is evaluated in this paper. This is done through three normalised parameters that represent the initial stiffness, post-yield stiffness, and strength of the column base, which can be independently adjusted. For these evaluations, a prototype steel building, which serves as a case study, is designed with sixteen different cases of a self-centering moment-resisting frame with different column base stiffness and strength characteristics (SC-MRF-CBs). A self-centering moment-resisting frame with conventional column bases and the same members and beam-column connections as those of the SC-MRF-CBs, named SC-MRF, serves as a benchmark frame. A set of 44 ground motions was used to conduct non-linear dynamic analyses and evaluate the seismic performance of the frames. Incremental dynamic analyses were also performed with the same ground motions set to evaluate the collapse capacity of the frames. Collapse capacity fragility curves and adjusted collapse margin ratios of the frames

¹ Corresponding author, E-mail address: V.Kamperidis@liverpool.ac.uk, ORCID ID number: 0000-0003-4893-7110.

31 were derived and used for the comparison of the seismic risk of the frames. The results show
32 that the new self-centering column base significantly improves the seismic performance of the
33 SC-MRF, demonstrating the potential of the SC-MRF-CBs to be redesigned with smaller
34 member sections. Moreover, the SC-MRF-CBs achieve significant reduction in collapse risk
35 compared to the SC-MRF. Finally, the results show that increasing the base strength and
36 stiffness improves the seismic performance and collapse capacity of the SC-MRF-CBs.

37 **KEYWORDS**

38 Column base; Self-centering; Collapse risk; Interstorey drifts and floor accelerations;
39 Parametric investigation; Seismic resilience

40 **1 INTRODUCTION**

41 Column bases have a very important role in the seismic response of steel moment-resisting
42 frames (MRFs) [1–5]. Eurocode 8 (EC8) [6] assumes that plastic hinges at the column base
43 connection will offer increased rotational ductility compared to other plasticity mechanisms
44 therein [7], such as column member plastic hinging. This strength-related code presumption
45 has been questioned by Lignos and Krawinkler [8], who showed that the ductility of the column
46 base plastic hinges may be compromised by local instabilities, leading to premature column
47 failure. Moreover, Aviram et al. [5] and Ruiz-García and Kanvinde [3] showed that decreasing
48 the initial stiffness of the base connections in low-rise buildings can change the height-wise
49 drift distribution, leading to drift and damage concentration and eventually to collapse. Zareian
50 and Kanvinde [2] showed that reducing the base fixity in low- to high-rise buildings can
51 increase the members' force demands, alter the global plastic mechanism, and significantly
52 reduce ductility, strength and collapse resistance. Torres-Rodas et al. [4] showed that increasing
53 the base flexibility of three-dimensional framed buildings, increases their transient drifts and
54 probabilities of collapse, while appreciably decreases their overstrength and ductility.

55 To address the deficiencies of MRFs under earthquakes, the self-centering MRFs (SC-MRFs)
56 were developed, such as those, for example, proposed in [9–16]. The main practice for SC-
57 MRFs is to use post-tensioned (PT) beam-column connections that utilise high-strength steel
58 tendons to clamp the beams to the columns and, thus, provide a re-centering mechanism that
59 can restore the initial geometry of the building up to a targeted seismic intensity. High-strength
60 steel is used to ensure that the tendons remain elastic up to the targeted frame response.
61 Therefore, in these SC-MRFs, the self-centering mechanism is provided through attaining a
62 targeted elastic elongation capacity for their PT tendons. Other researchers [17,18] have
63 provided self-centering mechanisms for their seismic-resilient MRFs by relying on fully
64 recoverable plastic deformations for the self-centering components of their systems up to as
65 targeted response level to eliminate the need for repair, i.e., by utilising superelastic shape
66 memory alloys (SMAs) for their self-centering components. The SC-MRFs with high-strength
67 PT tendons, which are of interest in this work, utilise energy dissipating devices (EDs) in their
68 PT beam-column connections to dissipate seismic energy and reduce the seismic forces and
69 accelerations [9]. These EDs can be easily removed or replaced, if damaged, which can
70 improve building’s resilience [19,20]. Combining these techniques, SC-MRFs can minimize
71 damage and residual drifts [10] and reduce peak drifts and floor accelerations [9,21].

72 Self-centering systems can offer an option of tuning the structural properties that fully define
73 their seismic hysteretic response. These properties are the initial stiffness, post-yield stiffness,
74 strength and energy dissipation. Different researchers have evaluated the effect of these
75 properties on the seismic response of different types of self-centering systems. Christopoulos
76 et al. [22,23] concluded that if adequate energy dissipation is provided in SDOF flag-shaped
77 response systems, these could have similar or improved peak drift response compared to that
78 of elastoplastic systems of the same initial stiffness and strength. It was highlighted, though,
79 that systems with self-centering response are prone to increased resonance vibration amplitudes

80 when their post-yield stiffness ratio, α (i.e., the ratio of the post-yield stiffness over the initial
81 stiffness), is increased [23]. Subsequently, Christopoulos et al. [24] found that the maximum
82 drift response of SDOF systems with self-centering response under the design basis earthquake
83 (DBE) [6] slightly decreases for increasing values of their post-yield stiffness. Interestingly,
84 this effect was reversed for the collapse prevention seismic performance level – a finding
85 fundamentally opposite to what applies in elastoplastic systems. Karavasilis and Seo [25]
86 concluded that increasing the strength and adding damping in self-centering SDOF systems,
87 generally decreases their peak total accelerations and displacements. In contrast, Cimellaro
88 [26] suggested that the drift response of a structure may be improved by adopting lower lateral
89 strength combined with higher damping ratios. Chou and Chen [27] investigated the
90 performance of SC-MRFs with either fixed or self-centering column bases under the DBE and
91 maximum considered earthquake (MCE) [28]. However, they did not assess the effect of the
92 base strength, stiffness and energy dissipation on the seismic response of their investigated
93 systems.

94 SC-MRFs with conventional column bases still cannot fully avoid structural damage and
95 residual drifts because of the plastic hinges developed at their column bases [9,10,27,29]. To
96 address this issue, SC-MRFs with self-centering column bases with replaceable/repairable EDs
97 (SC-MRF-CBs) were developed [27,29–33]. SC-MRF-CBs can eliminate damage at their
98 column bases and, thus, exhibit negligible residual drifts. Kamperidis et al. [29] have shown
99 that these systems significantly reduce the peak drifts compared to their correspondent SC-
100 MRFs, i.e., the frame with the same PT beam-column connections and same members with the
101 SC-MRF-CB, but with conventional rigid and full-strength column bases. In addition, the
102 design procedure proposed in [29] has the ability to fine-tune in a controlled manner the
103 strength, stiffness and hysteretic behaviour of a SC-MRF-CB, keeping these parameters
104 uncoupled. Thus, one can design an SC-MRF-CB adjusting these parameters in such a way that

105 its seismic response can be enhanced. However, an extensive and thorough parametric study
106 on the effects of these parameters to the seismic response of the SC-MRF-CBs is still missing.
107 Moreover, the performance-based design approach of modern structural codes [28,34]
108 mandates that buildings should be assessed against collapse as an extra measure of safety for
109 human life, on the top of satisfying the traditional force and displacement requirements of the
110 structural codes (e.g., EC8 [6]). This triggered research towards the collapse assessment of self-
111 centering systems. In line with this, Tzimas et al. [35] found that the collapse capacity of SC-
112 MRFs subjected to both far- and near-fault earthquakes, can be significantly improved by
113 adding viscous dampers. However, the collapse risk of the SC-MRF-CBs and their potential to
114 improve the collapse capacity of seismic-resistant steel buildings has never been evaluated.

115 This paper investigates the potential of SC-MRF-CBs equipped with the novel column base
116 proposed in the work of Kamperidis et al. [29] to further improve the seismic performance and
117 reduce the collapse risk of earthquake-resilient steel buildings equipped with SC-MRFs. The
118 collapse risk of these new systems has never been assessed before and, so, it is of particular
119 importance to investigate whether they attain a better or worse collapse behaviour compared to
120 the SC-MRF. By comparing both the seismic performance and collapse risk of the SC-MRF-
121 CBs with those of the SC-MRF, the performance of the former can be evaluated against all the
122 performance criteria modern structural codes demand. As such, it can be concluded whether
123 the SC-MRF-CBs can provide the potential to be designed for smaller steel members as
124 compared to those of the SC-MRF. However, the explicit consideration of an SC-MRF-CB
125 system with smaller cross-section than those of the SC-MRF is out of the scope of this work.
126 Moreover, the mainstream approach for the SC-MRFs is to be designed for similar strength
127 and initial stiffness with their correspondent conventional MRF [10,36], referred to as
128 correspondent MRF. Besides, due to the specific configuration of their PT beam-column
129 connections, SC-MRFs do not allow for flexible stiffness and strength frame adjustments. For

130 that reason, SC-MRFs are rather restricted to adhere to the above design approach. In contrast,
131 the self-centering column bases allow for the controlled adjustment of all the structural
132 properties that are necessary to fully determine their hysteretic behaviour to targeted predefined
133 levels through mathematical formulas [29]. This base structural properties' control mechanism
134 enables the adjustment of the stiffness and strength of the SC-MRF-CBs. A design procedure
135 for the self-centering column bases, which is enhanced compared to that in [29], is also
136 proposed. This work thoroughly and methodologically investigates for the first time the effects
137 of all the aforementioned base structural properties on the seismic performance and collapse
138 capacity of the SC-MRF-CBs for a given level of energy dissipation in their bases. The base
139 structural properties in question are the initial stiffness, post-yield stiffness, and strength,
140 represented through three normalised factors, which are described next (Section 3.1). For this
141 scope, a prototype steel building was designed that comprises different seismic-resistant
142 frames: i.e., an SC-MRF and sixteen SC-MRF-CBs with different base stiffness and strength
143 characteristics. The frames were modelled in OpenSees, where material and geometrical
144 nonlinearities were taken into account, along with strength and stiffness degradation. A set of
145 44 ground motions, scaled to three code-prescribed seismic intensity levels [6,28], was used to
146 conduct dynamic analyses and evaluate the seismic performance of the frames. In addition,
147 incremental dynamic analyses (IDAs) were performed with the same set of ground motions to
148 evaluate the collapse capacity of the frames. The collapse capacity fragility curves and the
149 adjusted collapse margin ratio of the frames were derived and used for the comparison of the
150 seismic risk of the frames.

151 **2 PROTOTYPE BUILDING**

152 The 5- by 3-bay, five-storey prototype steel building of [29], depicted in Figure 1, is utilised in
153 this work. Figure 1 shows the two identical braced frames in the *Y* direction and two identical
154 seismic-resistant frames in the *X* direction the building has at its perimeter. The building has

155 ductile non-structural elements and thus, the maximum interstorey drift ratio, $\theta_{s,max}$, must be
 156 less than 0.75% under the frequent occurred earthquake (FOE) in accordance with EC8 [6].
 157 The design spectrum of EC8 [6] with peak ground acceleration equal to 0.35g and ground type
 158 B was used for the design of the frame under the DBE.

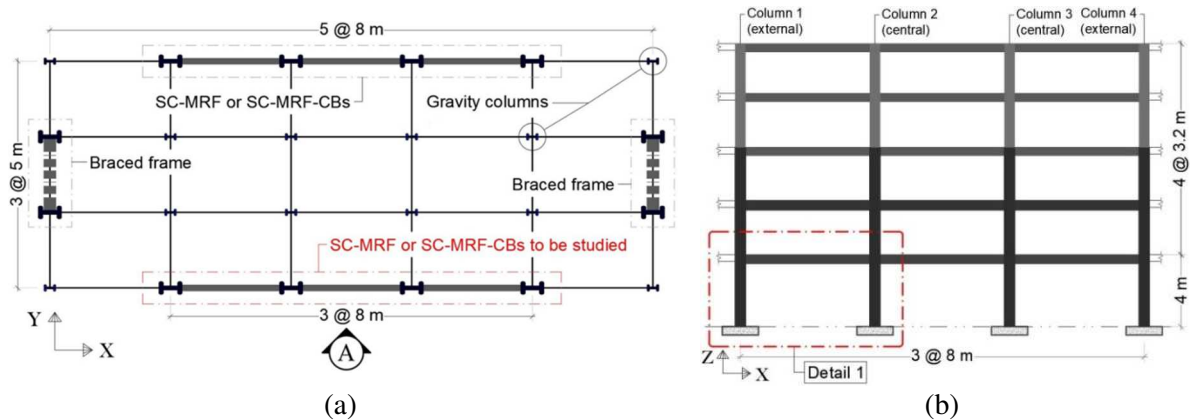
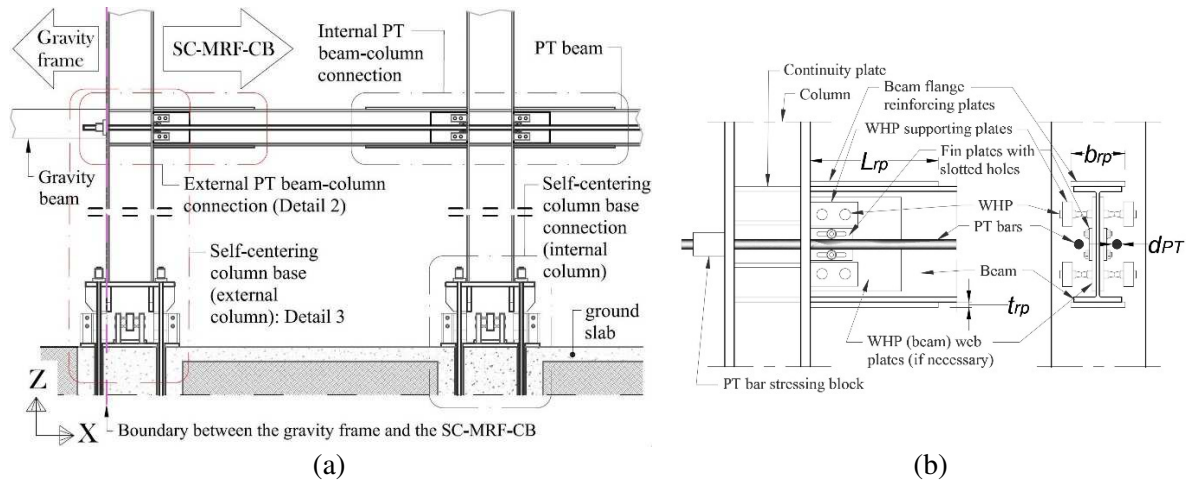


Figure 1 (a) Plan view; and (b) Elevation A of the prototype building.

159 Only the seismic-resistant frame of Elevation A of the prototype building, shown in Figure
 160 1(b), is studied in this work. The frame of interest was designed as: (a) an SC-MRF, following
 161 the design procedure of [10], to serve as the benchmark frame of this work; and (b) sixteen
 162 different SC-MRF-CBs with the self-centering column bases proposed in [29], having different
 163 base stiffness and strength characteristics but the same energy dissipation. The SC-MRF and
 164 all SC-MRF-CBs have the same beams, columns and PT beam-column connections. The
 165 design characteristics of the members and PT beam-column connections of the SC-MRF are
 166 those described in [35]. Figure 2(a) illustrates the bottom-left part of an SC-MRF-CB in
 167 Elevation A of the prototype building. The configurations of an external and internal (central)
 168 PT beam-column connection of the frames are depicted in Figure 2(a). Figure 2(b) shows a
 169 close-up view and the notation of these connections. The design procedure proposed in [29]
 170 was used for the design of the self-centering column bases of the SC-MRF-CBs.
 171
 172



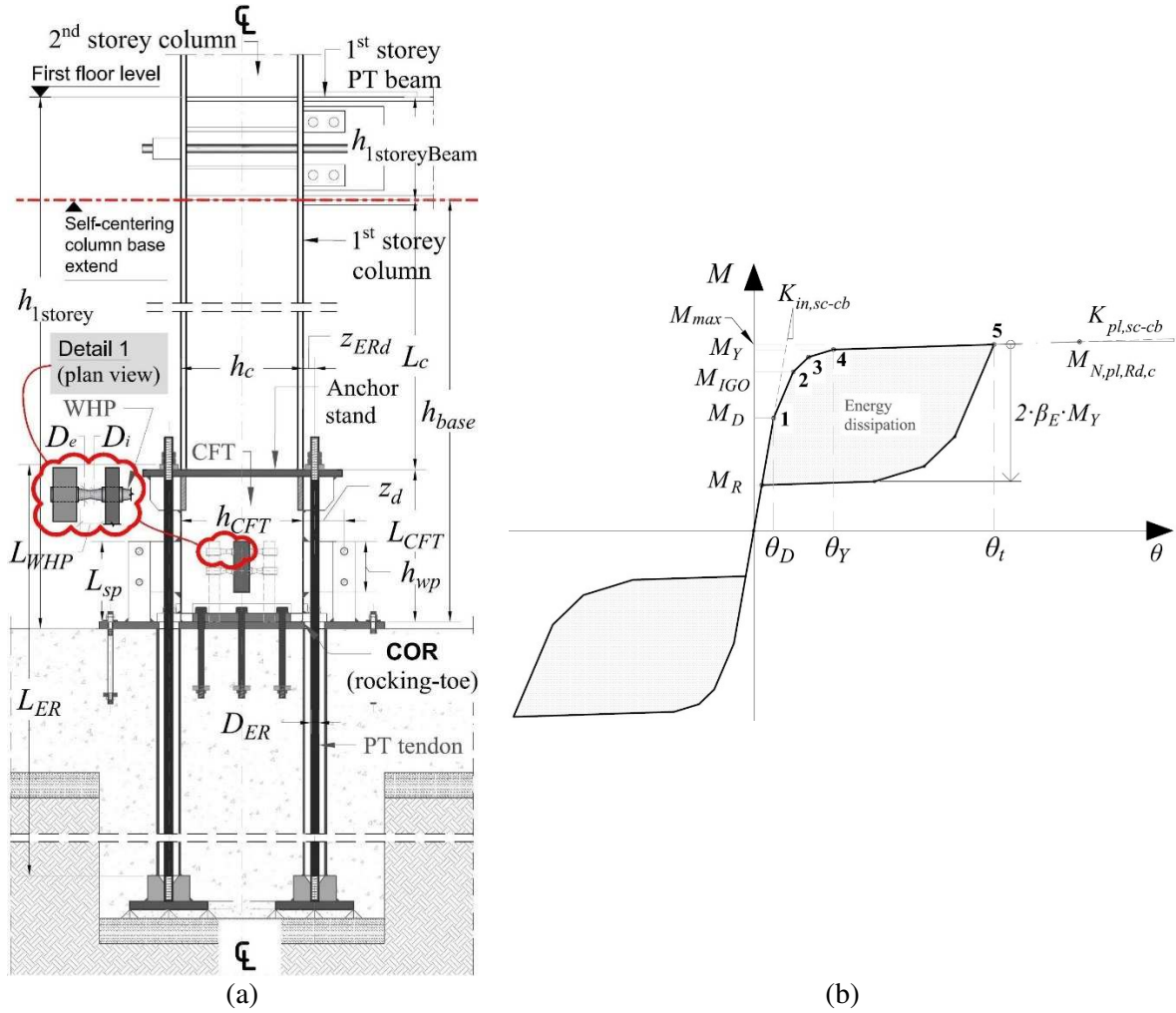
173 Figure 2 Close-up view of: (a) the bottom-left part of the SC-MRF-CB in Elevation A of the prototype
 174 building (Detail 1 in Figure 1(b)); and (b) PT beam-column connection at an external column with its
 175 notation (Detail 2 in Figure 2(a)).
 176

177 The web hourglass pins (WHPs) described in [13] were utilised as EDs in the column bases of
 178 the SC-MRF-CBs. The material of the WHPs was duplex stainless steel and its properties were
 179 as follows, as per [14]: yield stress equal to 543 MPa; ultimate stress equal to 778 MPa;
 180 elongation at fracture 34.25%; and Young's modulus equal to 227.848 GPa. The material for
 181 the multi-wire tendons of the self-centering column bases was the low-relaxation Grade 270
 182 steel material of ASTM A416 [37] with yield strength of 1676 MPa; ultimate tensile strength
 183 of 1860 MPa; Young's modulus equal to 195 GPa; and ultimate elongation 3.5%. This material,
 184 used in [38] and [39], is utilised in Section 4 for the fracture modelling of the tendons.

185 3 DESIGN CASES

186 Sixteen SC-MRF-CB design cases with different values for the strength, initial stiffness, and
 187 post-yield stiffness of their self-centering column bases are employed for the parametric study
 188 of this work. Thus, each self-centering column base employs a unique combination of values
 189 for these three base structural properties. There are three values of strength, three values of
 190 initial stiffness and five values of post-yield stiffness that are combined to form these sixteen
 191 combinations in the self-centering column bases. These values cover the whole range of
 192 feasible values that can be achieved each base structural property when designing the self-
 193 centering column utilising the design procedure proposed in [29]. The three ranges of feasible

194 values of the base structural properties are delimited by the given column cross-section and
195 column design loads, which serve as input for the aforementioned design procedure [29]. The
196 column and its design loads are derived from the elastic analysis and design of the
197 correspondent MRF, from which the SC-MRF-CBs' designs stem [29]; this will be further
198 explained next (Section 3.2). By examining self-centering column bases with base structural
199 properties that span the whole range of their feasible values, the limits of the distinct effect of
200 each one of these properties on the seismic response and collapse capacity of the SC-MRF-
201 CBs can effectively be determined. The notation of the self-centering column bases can be seen
202 in Figure 3(a). Each self-centering column base is considered to be a cantilevered assembly
203 that comprises the self-centering low-damage column base connection, proposed in [29], and
204 the steel column member of the first storey of the frame (Figure 3(a)). The self-centering
205 column base connections are determined by the height of the concrete-filled tube (CFT) (seen
206 in Figure 3(a)), L_{CFT} . The steel columns extend from the top of their self-centering base
207 connections up to the lower limit of the panel zones of the first-storey PT beam-column
208 connections. This limit is the level of the bottom flanges of the first-storey PT beams, as
209 indicated by the red dashed line in Figure 3(a). The steel columns are determined by their
210 length, L_c , as it is shown in Figure 3(a).



211 Figure 3 Self-centering column base: (a) configuration (Detail 3 in Figure 2(a)) and notation; and (b)
 212 theoretical moment (M)-rotation (θ) behaviour for an assumed clockwise bending moment and axial
 213 force.
 214

215 The rationale for considering this specific cantilevered assembly configuration as the means of
 216 assessing the base stiffness and strength of the SC-MRF-CBs is that it exclusively includes the
 217 only two elements that change in the whole configuration of the SC-MRF-CBs, i.e., the base
 218 connection and its connecting steel first-storey column. All the other parts of the frames are the
 219 same as those of the SC-MRF. Similar approaches have been adopted in previous relevant
 220 research [40]. Such an approach facilitates the large computational demands of this work. The
 221 theoretical moment (M)-rotation (θ) behaviour of the self-centering column bases can be seen
 222 in Figure 3(b). In this figure, θ is the chord rotation of the self-centering column bases, defined
 223 as the lateral displacement at the top of the column divided by the total height of the column
 224 bases, h_{base} . Thus, h_{base} is related with the geometry of the frame through the following relation:

225
$$h_{base} = h_{1storey} - h_{1storeyBeam} \quad (1)$$

226 where $h_{1storey}$ is the total height of the first storey and $h_{1storeyBeam}$ is the cross-sectional depth of
227 the beams of the first floor.

228 3.1 Investigated base structural properties

229 The investigated structural properties of the self-centering column bases (or simply base
230 structural properties) that are studied in this work are their strength, M_{IGO} , initial stiffness, $K_{in,sc-}$
231 cb , and post-yield stiffness, $K_{pl,sc-cb}$, which are described in Figure 3(b). M_{IGO} is the moment at
232 the first yielding of the WHPs of the self-centering column base connection (Figure 3(b)). M_{IGO}
233 is considered to represent the flexural strength of the self-centering column bases because the
234 strength of a system with metallic fuses should correspond to the point where the first yielding
235 of its structural fuses occurs [41]. The self-centering column base allows the controlled
236 adjustment of these base structural properties by utilising the analytical expressions that are
237 presented next. To uncouple the research findings of this work from the specific design
238 characteristics of the frames studied herein (e.g., the size of the first-storey columns, the cross-
239 sectional depth of which, denoted as h_c (see Figure 3(a)), and its plastic moment of resistance,
240 $M_{N,pl,Rd,c}$ (described in Eq. (3), below), are of interest in this study), the base structural
241 properties are represented by the following normalised parameters: (a) the strength ratio, η ; (b)
242 the normalised initial base stiffness factor, β_{base} ; and (c) the post-yield stiffness ratio, α . Thus,
243 the findings of this work can be extended to any SC-MRF-CB that is designed as per the design
244 procedure proposed in [29].

245 Likewise previous research [25,42], the energy dissipation factor, β_E , is utilised to control the
246 energy dissipation in all sixteen self-centering column bases. β_E was selected to take the same,
247 near-maximum allowable value to allow the self-centering behaviour of the column bases and
248 maximise their seismic energy dissipation. Thus, β_E was not included in the parametric study.
249 Based on previous relevant research [22,23,43], it was hypothesized that by maximising the

250 energy dissipation at the column bases, the seismic response and collapse capacity of the SC-
 251 MRF-CBs would be optimally improved. Because the upper bound of β_E equals 0.5 [25,42], β_E
 252 was conservatively taken equal to 0.48 in all self-centering column bases. The energy
 253 dissipation in each self-centering column base is due to the energy dissipated by the WHPs up
 254 to the target base rotation, θ_t (Figure 3(b)); the steel columns were intended to remain elastic
 255 and not contribute to the energy dissipation of the self-centering column bases. For this
 256 research, θ_t was conservatively chosen to be equal to the rotation capacity limit of EC8 for
 257 ductility class high MRFs, i.e., 0.035 radians [6]. This implies that no strength and stiffness
 258 deterioration was expected to take place up to θ_t . β_E was defined as:

$$259 \quad \beta_E = \frac{M_Y - M_D}{M_Y} \quad (2)$$

260 where M_Y is the moment of the self-centering column bases when all WHPs have reached their
 261 elastic limit; and M_D is the decompression moment of the self-centering connection, i.e., the
 262 moment at which the gap at the rocking interface of the column base opens [10,29]. These
 263 characteristic moments, along with their corresponding rotations, can be seen in Figure 3(b).

264 The strength factor, η , was defined as:

$$265 \quad \eta = \frac{M_{IGO}}{M_{N,pl,Rd,c}} \quad (3)$$

266 where M_{IGO} is the moment at the first yielding of the WHPs of the self-centering column base
 267 connection; $M_{N,pl,Rd,c}$ is the plastic moment of resistance of the column. $M_{N,pl,Rd,c}$ accounts for
 268 interaction with the design axial force, N_{Ed} , and the overstrength of the connections materials
 269 and for other material effects, in accordance with EC8 [6] and Eurocode 3 (EC3) [44]
 270 provisions. N_{Ed} is the axial force derived from the analysis of the correspondent MRF for the
 271 gravity loads combination of actions [29]. The strength factor η consists a measure of the
 272 strength of the base connection but can represent the strength of the whole self-centering

273 column base because the former is the only part of the latter that is expected to yield up to θ_i .
 274 The concept that the strength factor η consists a measure of the column bases' strength was
 275 adopted on the basis that it relates the yield strength of the base connections with that of the
 276 column member. This is in line with the relevant provisions of Eurocode 3 [45] that classify
 277 moment-resisting connections with respect to their strength by comparing the strength of the
 278 connections with the strength of their connecting members. Previous research on PT beam-
 279 column connections [10] has set out an upper limit for η equal to unity. The parametric
 280 investigation of this work shown that to achieve self-centering and damage-control behaviour
 281 up to θ_i , only values of η below 0.45 were capable of yielding self-centering column base
 282 designs with initial and post-yield stiffness within their feasible range of values; these latter
 283 two base structural properties were controlled through their normalised factors, β_{base} and α ,
 284 respectively, described next. For that reason, the three values of η this work examined were
 285 0.30, 0.35 and 0.40.

286 The normalised initial base stiffness factor, β_{base} , was defined as:

$$287 \quad \beta_{base} = \frac{K_{in,sc-cb}}{K_{in,conv}} \quad (4)$$

288 where $K_{in,conv}$ is the initial (elastic) flexural stiffness of a cantilever-fixed steel column of total
 289 height equal to h_{base} ; and $K_{in,sc-cb}$ the initial stiffness of a self-centering column base, assumed
 290 equal to the elastic flexural stiffness of the steel cantilevered column on the top of the self-
 291 centering column base connection, $K_{el,col}$, since the initial stiffness of the latter connection is
 292 taken as infinite [29]. Thus, $K_{el,col}$ is calculated for a column height of L_c . For the self-centering
 293 column bases under investigation, the three β_{base} values examined were 133%, 167% and 200%.

294 The post-yield stiffness ratio, α , was defined according to the following relation:

$$295 \quad \alpha = \frac{K_{pl,sc-cb}}{K_{in,sc-cb}} \quad (5)$$

296 where $K_{pl,sc-cb}$ is the post-yield stiffness of the self-centering column base, defined as:

$$297 \quad K_{pl,Sc-Bc} = \frac{K_{pl,sc-cb} \cdot K_{el,col}}{K_{pl,sc-cb} + K_{el,col}} \quad (6)$$

298 where $K_{pl,sc-cb}$ is the post-yield stiffness of the self-centering column base connection, which
 299 was determined by the following relation [29]:

$$300 \quad K_{pl,sc-cb} = K_{fe} \cdot \left(\lambda \cdot n_{WHPu} \cdot z_u^2 + \lambda \cdot n_{WHPc} \cdot z_c^2 + \lambda \cdot n_{WHPd} \cdot z_d^2 \right) + K_{ER} \cdot \left(n_{ERu} \cdot z_{ERu}^2 + n_{ERd} \cdot z_{ERd}^2 \right) \quad (7)$$

301 where k_{fe} is the elastic stiffness of a single WHP [29]; λ equals 2% according to [29]; n_{WHPu} and
 302 n_{WHPd} are the numbers of the WHPs at the gap-opening and rocking-toe side of the self-
 303 centering column base connections (the rocking toe coincides with the centre of rotation of the
 304 connection (COR), as it is seen in Figure 3(a) for an assumed clockwise moment); n_{WHPc} the
 305 number of the central WHPs; z_u , z_d and z_c , the lever arms of the WHPs at the gap-opening side,
 306 rocking-toe side and that of the central WHPs, respectively; K_{ER} is the elastic axial stiffness of
 307 each tendon, equal to $E_{ER} \cdot A_{ER} / L_{ER}$, with E_{ER} , A_{ER} and L_{ER} the tendon's material Young's
 308 modulus, cross-sectional area and length, respectively; and n_{ERu} and n_{ERd} , and z_{ERu} and z_{ERd} the
 309 number and lever arms of the PT tendons at the gap-opening and rocking-toe side of the self-
 310 centering column base, respectively. The lever arms z_d and z_{ERd} , are defined in Figure 3(a). The
 311 lever arms z_u and z_{ERu} were derived by adding to z_d and z_{ERd} the cross-sectional depth of the
 312 CFT, h_{CFT} , respectively. z_c equals $h_{CFT}/2$. Five different values of α were examined in this work,
 313 i.e., 5%, 10%, 15%, 20% and 24.5%. The value of 24.5% was the maximum value of α obtained
 314 for the given level of strength and initial stiffness of the relevant self-centering column base.
 315 This is in agreement with the maximum achievable limit of α for real flag-shaped response
 316 systems, determined to about 25%, proposed by Wiebe and Christopoulos [46].

317 3.2 Self-centering column base design procedure

318 This section presents the design procedure utilised to derive the sixteen self-centering column
319 base designs that are investigated in this work. The design procedure is that described in the
320 work of Kamperidis et al. [29], with the only difference being that – in this work – the
321 investigated base structural properties are given pre-selected values utilising Eq. (2) through
322 (7) of Section 3.1. Pre-selecting these values, reduces the number of unknowns to be
323 determined (as compared to the approach adopted in [29]), significantly facilitating the design
324 process. To minimize repetition since the design procedure in [29] has been presented therein
325 in detail, the design approach adopted in this work presents only limited mathematical formulas
326 from [29].

327 To initiate the design procedure, the following input quantities are required: the column axial
328 force, N_{Ed} ; the column cross-section, so that its cross-sectional depth, h_c , and plastic moment
329 of resistance, $M_{N,plRd,c}$, are determined; and the target base rotation, θ_t . The design procedure
330 comprises the following steps:

331 Step 1: Design the tendons

- 332 (a) Select a value for β_{base} and calculate $K_{in,sc-cb}$ from Eq. (4). From $K_{in,sc-cb}$, L_c is derived
333 utilising the relevant elastic flexural stiffness formula from mechanics (Section 3.1).
334 From Figure 3(a) and given the resulted L_c value, h_{CFT} can be derived.
- 335 (b) Select a value for the strength factor, η . From Eq. (3) M_{IGO} can then be derived.
- 336 (c) Select a value for the ratio M_D/M_{IGO} so that it is larger than 0.5, but as closer as it gets
337 to that latter value. This is to ensure self-centering capability but also to maximize
338 energy dissipation. Thus, M_D is derived.
- 339 (d) Select a number, $n_{ERu}=n_{ERd}$, and a lever arm for the tendons, e.g., z_{ERd} (z_{ERu} can be
340 determined as per Section 3.1). It is suggested that four tendons are placed at the corners

341 of the anchor stand, which is the elevated stiff plate welded on the top of the CFT (see
 342 Figure 3(a)); i.e., $n_{ERu}=n_{ERd}=2$. Then, calculate the initial post-tensioning force at each
 343 tendon, T , as per Eq. (2) of Kamperidis et al. [29].

344 (e) Select an appropriate high-strength steel grade material for the tendons, e.g., Grade 270
 345 steel material of ASTM A416, to ensure a high yield strength, $f_{y,ER}$, for the tendons, and
 346 assume a diameter for them, D_{ER} (this determines A_{ER}). Then, utilize Eq. (3) of [29] to
 347 calculate L_{ER} . Also, approximate the moment contribution of the tendons for the
 348 characteristic rotation, θ_2 , denoted as $M_{ER}(\theta_2)$, as per Eq. (7) of [29]. θ_2 is the rotation
 349 at which the first WHP of the self-centering column base yields. $M_{ER}(\theta_2)$ is to be used
 350 next.

351 Step 2: Design the WHPs

352 (a) Select a number for the WHPs at each side of the self-centering column base (e.g.,
 353 n_{WHPd}). It is suggested that two WHPs are placed at all sides of the column base; this is
 354 for construction practicality and to ensure that the column base control its structural
 355 properties over both of its main axes [29]; i.e., $n_{WHPd}=n_{WHPc}=n_{WHPu}=2$. Also, select a
 356 lever arm for the WHPs, e.g., z_d (z_u and z_c can be determined as per Section 3.1). Then,
 357 calculate the yield strength of a single WHP, $F_{y,WHPi}$, as per Eq. (5) of [29], utilising
 358 $M_{ER}(\theta_2)$ from Step 1(e). The internal diameter of the WHPs, D_i (described in Detail 1
 359 of Figure 3(a)), can then be calculated from the following relation as per [10,29]:

$$360 \quad D_i = \sqrt{\frac{2 \cdot F_{y,WHPi} \cdot \sqrt{3}}{\pi \cdot f_{y,WHP}}} \quad (8)$$

361 where $f_{y,WHP}$ is the yield strength of the material of the WHPs.

362 (b) Select a value for α , and based on Eq. (5) and the value of $K_{in,sc-cb}$ derived from Step
 363 1(a), calculate $K_{pl,sc-cb}$. Based on the $K_{pl,sc-cb}$ value, calculate the WHPs' elastic stiffness

364 K_{fe} from Eq. (7). Moreover, to derive a relationship between the length of the tapered
 365 part of half a WHP, L_{WHP} , and the external diameter of the WHP, D_e , substitute D_i from
 366 Eq. (8) into the following relationship [29,47]:

$$367 \quad L_{WHP} = \frac{2.566 \cdot D_e^3}{\pi \cdot D_i^2} \quad (9)$$

368 Both L_{WHP} and D_e are described in Detail 1 of Figure 3(a). A second relationship between
 369 L_{WHP} and D_e , can be derived by substituting K_{fe} from above and D_i from Eq. (8) into the
 370 following relationship [13,29]:

$$371 \quad K_{fe} = 2 \cdot \frac{9 \cdot \pi \cdot D_e^3 \cdot D_i \cdot E_{WHP} \cdot G_{WHP}}{40 \cdot E_{WHP} \cdot D_e^2 \cdot L_{WHP} + 48 \cdot G_{WHP} \cdot L_{WHP}^3} \quad (10)$$

372 where E_{WHP} and G_{WHP} are the elastic and shear moduli of the WHP material. Solving the
 373 system of Eqs. (9) and (10), the values of D_e and L_{WHP} can be derived.

374 Step 3: Check the self-centering capability of the column base and the column plastic hinge
 375 avoidance

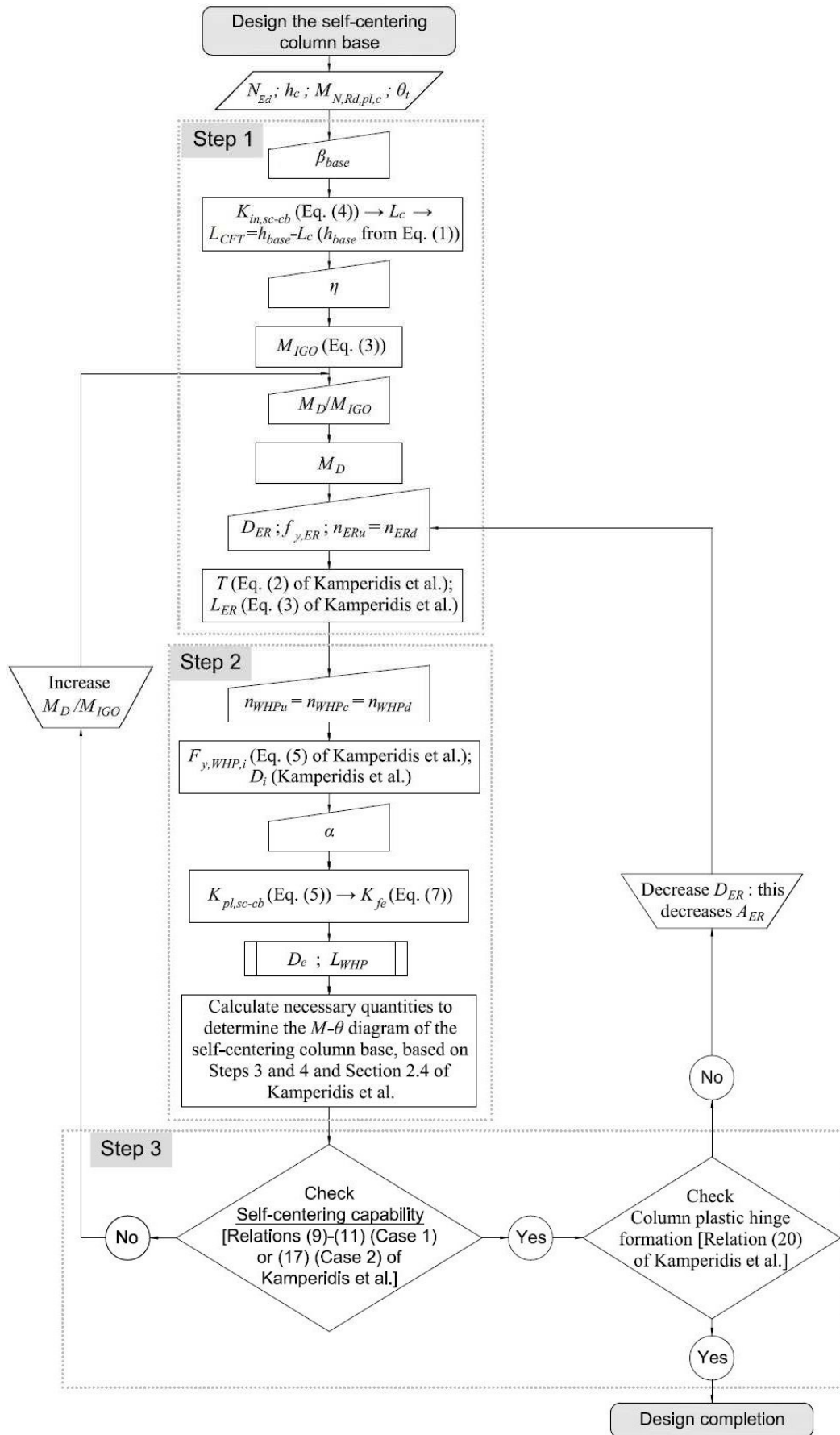
376 The self-centering capability of the column bases is checked by utilising Relationships (9)
 377 through (11) and Relationship (17) from [29]. There are two cases:

378 (a) If self-centering behaviour is achieved, then proceed with checking whether a plastic
 379 hinge is formed at the bottom of the column member. This is done by utilising
 380 Relationship [20] of [29]. Two case are now identified:

- 381 1. A plastic hinge is formed: in this case, decrease A_{ER} in Step 1(e) by be employing a
 382 smaller tendon (smaller D_{ER}), and repeat all steps up to this point until this check is
 383 satisfied. Then finalize the procedure.
- 384 2. A plastic hinge is not formed: in this case, finalize the design process.

385 (b) If self-centering behaviour is not achieved, return to Step 1(c) and increase the ratio
386 M_D/M_{IGO} . Then, repeat the design procedure up to Step 3(a) until self-centering is
387 achieved and plastic hinge is not formed at the column. When Step 3(a) is fully
388 satisfied, complete the design process.

389 The design steps are summarized in the flowchart of Figure 4.



390
391

Figure 4 Flowchart of the design approach of the self-centering column bases, based on the design procedure proposed in Kamperidis et al. [29].

392 3.3 Self-centering column base designs

393 Table 1 lists the normalised base structural properties of the sixteen self-centering column base
 394 designs and Table 2 presents their key design characteristics. These design characteristics were
 395 derived utilising the design procedure presented in Section 3.2. The notation utilised in Table
 396 2 is described in Figure 3(a) (and its Detail 1) and in Section 3.2.

397 Table 1. Normalised base structural properties of the sixteen self-centering column bases.

| Frame | η | β_{base} (%) | α (%) |
|------------|--------|--------------------|--------------|
| H40K133A5 | 0.4 | 133 | 5 |
| H40K133A15 | 0.4 | 133 | 15 |
| H40K167A15 | 0.4 | 167 | 15 |
| H40K167A5 | 0.4 | 167 | 5 |
| H40K133A10 | 0.4 | 133 | 10 |
| H40K167A10 | 0.4 | 167 | 10 |
| H40K133A24 | 0.4 | 133 | 24.5 |
| H35K133A5 | 0.35 | 133 | 5 |
| H35K133A15 | 0.35 | 133 | 15 |
| H35K167A15 | 0.35 | 167 | 15 |
| H35K167A5 | 0.35 | 167 | 5 |
| H35K133A10 | 0.35 | 133 | 10 |
| H35K167A10 | 0.35 | 167 | 10 |
| H35K200A10 | 0.35 | 200 | 10 |
| H35K133A20 | 0.35 | 133 | 20 |
| H30K133A10 | 0.30 | 133 | 10 |

398
 399 Table 2. Key column base design characteristics of the sixteen SC-MRF-CBs.

| Frame | L_{WHP} (m) | D_e (m) | D_i (m) | $F_{y,WHP,i}$ (kN) | K_{fe} (MN/m) | L_{sp} (m) | h_{wp} (m) | L_{ER} (m) | D_{ER} (m) | z_d (m) | $z_{ER,d}$ (m) | L_{CFT} (m) | T (kN) |
|------------|------------------|--------------|--------------|-----------------------|--------------------|-----------------|-----------------|-----------------|-----------------|--------------|-------------------|------------------|-------------|
| H40K133A5 | 0.12 | 0.04 | 0.02 | 161.78 | 109.22 | 0.37 | 0.24 | 7.49 | 0.02 | 0.24 | 0.09 | 0.44 | 262.70 |
| H40K133A15 | 0.07 | 0.03 | 0.02 | 156.39 | 260.19 | 0.33 | 0.21 | 7.47 | 0.02 | 0.26 | 0.16 | 0.44 | 271.41 |
| H40K167A15 | 0.06 | 0.03 | 0.02 | 158.54 | 307.41 | 0.33 | 0.20 | 7.39 | 0.02 | 0.24 | 0.37 | 0.73 | 273.25 |
| H40K167A5 | 0.21 | 0.05 | 0.02 | 151.38 | 38.68 | 0.40 | 0.27 | 9.59 | 0.02 | 0.25 | 0.38 | 0.73 | 228.89 |
| H40K133A10 | 0.06 | 0.04 | 0.02 | 166.28 | 357.10 | 0.33 | 0.20 | 8.50 | 0.02 | 0.21 | 0.15 | 0.44 | 274.02 |
| H40K167A10 | 0.10 | 0.04 | 0.02 | 132.46 | 122.24 | 0.34 | 0.22 | 7.62 | 0.02 | 0.42 | 0.37 | 0.73 | 261.05 |
| H40K133A24 | 0.06 | 0.03 | 0.02 | 163.63 | 396.73 | 0.32 | 0.20 | 5.52 | 0.03 | 0.19 | 0.10 | 0.44 | 281.83 |
| H35K133A5 | 0.12 | 0.04 | 0.02 | 136.90 | 89.09 | 0.36 | 0.23 | 7.58 | 0.02 | 0.27 | 0.12 | 0.44 | 204.77 |
| H35K133A15 | 0.06 | 0.04 | 0.02 | 142.89 | 264.52 | 0.32 | 0.20 | 6.64 | 0.02 | 0.22 | 0.16 | 0.44 | 212.16 |
| H35K167A15 | 0.06 | 0.03 | 0.02 | 100.44 | 189.61 | 0.30 | 0.18 | 7.32 | 0.02 | 0.56 | 0.36 | 0.73 | 212.51 |
| H35K167A5 | 0.19 | 0.04 | 0.02 | 125.10 | 34.27 | 0.38 | 0.26 | 8.73 | 0.02 | 0.27 | 0.38 | 0.73 | 171.44 |
| H35K133A10 | 0.08 | 0.04 | 0.02 | 142.58 | 184.52 | 0.34 | 0.21 | 6.35 | 0.02 | 0.23 | 0.16 | 0.44 | 207.34 |
| H35K167A10 | 0.05 | 0.04 | 0.02 | 88.76 | 184.92 | 0.30 | 0.17 | 8.65 | 0.02 | 0.70 | 0.36 | 0.73 | 215.25 |
| H35K200A10 | 0.06 | 0.04 | 0.02 | 125.24 | 251.67 | 0.31 | 0.19 | 8.70 | 0.02 | 0.34 | 0.50 | 0.91 | 212.51 |
| H35K133A20 | 0.06 | 0.03 | 0.02 | 113.55 | 252.32 | 0.31 | 0.18 | 7.64 | 0.03 | 0.44 | 0.13 | 0.44 | 212.51 |
| H30K133A10 | 0.06 | 0.03 | 0.02 | 104.64 | 212.41 | 0.30 | 0.18 | 5.99 | 0.03 | 0.37 | 0.15 | 0.44 | 151.00 |

401 4 NON-LINEAR MODELS

402 The OpenSees platform [48] was used to model the prototype SC-MRF and SC-MRF-CBs.
403 The PT beam-column connections in all frames were modelled as in [35]. The columns and the
404 length of the beams that is reinforced were modelled with beam-column fiber elements that
405 exhibit bi-linear elastoplastic stress-strain behaviour. Force-based beam-column fiber elements
406 with end hinges [49] were used for the un-reinforced lengths of the beams. The stress-strain
407 cyclic behaviour of the fibers was modelled by utilising the modified Ibarra-Krawinkler model
408 [50]. This model was used because it captures the strength and stiffness degradation resulting
409 from beam local buckling observed after the end of the beam flange reinforcing plates. This
410 type of modelling was used in [51] and results in hysteretic curves for flexural members that
411 are smooth and similar to the ones observed in experiments. The Ibarra-Krawinkler model does
412 not take into account the effect of a variable axial force on the bending deterioration parameters
413 [51]. The use of fiber elements results in reductions of the bending strength of the beam-column
414 elements due to the variable axial-moment interaction [51]. Thus, this approach also captures
415 the axial force (caused by the PT force at the tendons) – bending moment interaction in the
416 beams of the frames [35,51]. Panel zones are modelled based on [52]. The OpenSees model
417 developed in [29] is used for the column bases of the SC-MRF-CBs. The gravity columns of
418 the tributary area of the frames are modelled as three lean-on columns to take into account P-
419 Δ effects. Truss elements that connect the nodes of the lean-on columns to nodes defined along
420 the length of the beams at the points where the secondary beams are placed are used to model
421 diaphragm action of the composite slabs. The diaphragm also helps to avoid the shortening of
422 the PT beams (as these are seen in Figure 2(a)) due to the increase of the post-tensioning forces
423 caused by to the connections' gap opening and closing during seismic loads (the PT beams are
424 only resist the constant axial force caused by the initial post-tensioning of their PT bars [10]).
425 The stiffness of these trusses is 100 times larger than that of the axial stiffness of the beam. By

426 connecting separately each bay's secondary beam nodes with the corresponding lean-on
 427 column node of the same storey, these stiff truss elements help to model the discontinuity
 428 between the composite slabs that correspond to each different bay of the self-centering system,
 429 as per the tributary area of the bay. Discontinuity between the composite slab and the flanges
 430 of the columns of the self-centering system is also assumed for the floor system utilised in this
 431 work [53]. The aim of the above floor system discontinuities is to avoid that the PT beam be
 432 restrained by the composite slab (minimizing the damage in the slab also); allow the free gap
 433 opening and closing of the PT connection (thus, not affecting the connection's hysteretic
 434 behaviour) [10,53]; and allow for the unobstructed self-centering frame expansion [10,36].
 435 More details on the adopted floor system can be found in [10,53,54]. The tendons of the column
 436 bases were modelled to fracture to more accurately simulate the actual collapse limit of the
 437 frames under investigation. To this purpose, the Fatigue material of OpenSees [48] was utilised
 438 in conjunction with the parent material of the tendons. The parent material of the tendons is the
 439 material around which the Fatigue material is wrapped [48], and which in this case is the
 440 material steel01 of OpenSees [48]. The material steel01 has a bilinear elastoplastic hysteresis
 441 with post-stiffness ratio equal to 0.03 [29]. The Fatigue material is wrapped around the steel01
 442 material without altering the stress-strain relationship of the latter [48]. The Fatigue material
 443 utilises the Coffin-Manson relationship [55] and the Palmgren-Miner linear damage
 444 accumulation rule [55] to model their low-cycle fatigue and fracture. The Coffin-Manson rule
 445 is expressed by the relationship:

$$\frac{\Delta \varepsilon_p}{2} = \varepsilon'_f \cdot (2 \cdot N_f)^m \quad (11)$$

447 where $\frac{\Delta \varepsilon_p}{2}$ is the plastic strain amplitude; ε'_f the fatigue ductility coefficient, which represents
 448 the intersect of the plastic asymptotic line of the Coffin-Manson curve in the log-log space, i.e.,
 449 the strain at which one cycle will cause failure (fracture) [55,56]; N_f the number of the full

450 cycles to failure (or $2 \cdot N_f$ the number of load reversals to failure); and m the fatigue ductility
451 exponent, which represents the sensitivity of the log of the strain amplitude to the log of N_f
452 [56], i.e., the slope of the Coffin-Manson curve in the log-log space. For the Fatigue material
453 of the tendons, ε_f' was taken equal to 4%. This strain value is a conservative fracture value as:
454 (a) it represents the initial wire fracture of the strands of the tendons, ignoring the appreciable
455 strength reserve that remains at the tendons afterwards and through the fracture of all their
456 wires [38,39]; (b) it considers the premature fracture of the tendons due to excessive stress
457 concentration at the vicinity of their anchors, as per the work of Bruce and Eatherton [38],
458 where the fracture value in question represents the average observed first-wire fracture limit
459 (not the relevant proposed design limit) from their tested specimens, considering both the
460 tendon materials used therein, and also a newer multiple-use barrel and wedge anchorage
461 system that allowed for larger inelastic strains prior to initial wire fracture, compared to the
462 traditional barrel and wedge anchorage system that the authors also tested in their work; (c) it
463 represents the upper first-wire fracture limit attained from the tested specimens in the work of
464 Sideris et al. [39], given that their observed strain fracture values ranged from 1.5% to 4%; and
465 (d) it is a value much smaller than those provided by these tendons manufacturers, i.e., 6-7%
466 [57]. The fatigue ductility exponent, m , for the Fatigue material of OpenSees, was taken equal
467 to -0.458, as per the work of Uriz [56]. For the maximum values of strain to be set out in the
468 model of the material, the suggested minimum and maximum values of $-1e16$ and $1e16$,
469 respectively, have been adopted [48]. To accumulate damage in the material due to the random
470 strain amplitude excursions during an earthquake, the Fatigue material of OpenSees utilises a
471 rainflow method [55] counting algorithm to count the number of cycles at various strain
472 amplitudes, in conjunction with the Palmgren-Miner's linear damage accumulation Rule [55].
473 The Palmgren-Miner's Rule is expressed by the damage index, D , which is given by the
474 following mathematical formula:

$$D = \sum_{i=1}^j \frac{n_i}{N_{f,i}} \quad (12)$$

476 where $N_{f,i}$ is the number of cycles that can be resisted by the material until failure at the i th
 477 constant strain amplitude loading, in a total of j such loadings with constant strain amplitudes;
 478 and n_i is the number of loading cycles the material has undergone at the i th constant strain
 479 amplitude loading [55]. Once index D in the Fatigue material reaches the value of 1.0, the force
 480 (or stress) in the parent material becomes zero, signalling the failure of the parent material [48].

481 The fracture of the WHPs was not modelled in this study, as, based on previous experimental
 482 and numerical studies [14,54,58], their geometry and position around the column bases can be
 483 selected to avoid fracture before the building's seismic collapse due to second order effects
 484 [51].

485 **5 NON-LINEAR DYNAMIC ANALYSES**

486 The set of the far-fault ground motions of FEMA P695 [59] was used for the non-linear
 487 dynamic analyses of this study. This set comprises 22 record pairs, each with two horizontal
 488 components for a total of 44 records. The ground motions of the above set were recorded on
 489 stiff soil and at sites with distance larger than or equal to 10 km from fault rupture. The
 490 magnitudes of the earthquakes range from M 6.5 to M 7.6 with an average magnitude of M 7.0.
 491 The records were scaled to DBE and MCE, using as intensity measure (IM) the 5% spectral
 492 acceleration at fundamental period T_1 of the frame models, $S_a(T_1)$.

493 *5.1 Assessment of the seismic performance of the frames*

494 The results of the 44 non-linear dynamic analyses for the SC-MRF and sixteen SC-MRF-CBs
 495 were post-processed and the median maximum values of $\theta_{s,max}$ of all the storeys and peak floor
 496 acceleration (PFA) from all the floors are shown in Table 3. The results in Table 3 indicate that
 497 the $\theta_{s,max}$ of all SC-MRF-CBs is lower than that of the SC-MRF under the FOE, DBE and MCE
 498 seismic intensity levels. In particular, for the FOE intensity level, the relative reduction of the

499 $\theta_{s,max}$ of the SC-MRF-CBs compared to that of the SC-MRF ranges from 3.03% for the
500 H35K167A5 to 23.65% for the H35K167A10. Under the DBE, the relevant minimum
501 reduction of $\theta_{s,max}$ is 1.42% and achieved for the H35K133A5 and the maximum is 24.13% and
502 achieved for the H40K167A15. Under the MCE, the H35K133A5 achieves the minimum
503 reduction of $\theta_{s,max}$ equal to 0.95% and the H35K167A10 the maximum equal to 18.55%.
504 Moreover, all the SC-MRF-CBs achieve $\theta_{s,max}$ lower than the “life safety” and “collapse
505 prevention” limits of EC8 [6] and ASCE/SEI 41-06 [60]. As it can be seen from Table 3, the
506 SC-MRF-CBs achieve as much as a 24.05% overall $\theta_{s,max}$ reduction (minimum reduction
507 between all seismic intensity levels for the H35K167A10). These results demonstrate that the
508 new column base configuration is very effective in reducing $\theta_{s,max}$, and that is done by only
509 adjusting its base stiffness and strength characteristics.

510 Table 3. Median maximum values of $\theta_{s,max}$ of all the storeys and PFA from all the floors of the
511 SC-MRF and SC-MRF-CB design cases.

| Frame | Fundamental Period T_1 (s) | $\theta_{s,max}$ (%) | | | PFA (g) | | |
|------------|---------------------------------|----------------------|-------|-------|---------|-------|-------|
| | | FOE | DBE | MCE | FOE | DBE | MCE |
| SC-MRF | 0.94 | 0.655 | 1.814 | 2.623 | 0.499 | 1.043 | 1.487 |
| H40K133A5 | 0.95 | 0.547 | 1.667 | 2.416 | 0.506 | 0.980 | 1.481 |
| H40K133A15 | 0.95 | 0.530 | 1.529 | 2.336 | 0.534 | 0.932 | 1.385 |
| H40K167A15 | 0.93 | 0.519 | 1.376 | 2.170 | 0.521 | 0.932 | 1.362 |
| H40K167A5 | 0.93 | 0.621 | 1.671 | 2.494 | 0.520 | 1.036 | 1.462 |
| H40K133A10 | 0.95 | 0.530 | 1.510 | 2.319 | 0.526 | 0.918 | 1.356 |
| H40K167A10 | 0.93 | 0.531 | 1.433 | 2.264 | 0.542 | 0.954 | 1.316 |
| H40K133A24 | 0.95 | 0.530 | 1.448 | 2.294 | 0.519 | 0.919 | 1.508 |
| H35K133A5 | 0.95 | 0.576 | 1.788 | 2.598 | 0.509 | 0.911 | 1.428 |
| H35K133A15 | 0.95 | 0.542 | 1.655 | 2.353 | 0.506 | 0.918 | 1.341 |
| H35K167A15 | 0.93 | 0.501 | 1.384 | 2.147 | 0.489 | 0.903 | 1.416 |
| H35K167A5 | 0.93 | 0.635 | 1.745 | 2.538 | 0.556 | 0.966 | 1.418 |
| H35K133A10 | 0.95 | 0.546 | 1.683 | 2.379 | 0.495 | 0.910 | 1.392 |
| H35K167A10 | 0.93 | 0.500 | 1.396 | 2.136 | 0.494 | 0.899 | 1.400 |
| H35K200A10 | 0.91 | 0.506 | 1.534 | 2.140 | 0.504 | 0.887 | 1.367 |
| H35K133A20 | 0.95 | 0.522 | 1.542 | 2.299 | 0.515 | 0.914 | 1.364 |
| H30K133A10 | 0.95 | 0.543 | 1.667 | 2.299 | 0.470 | 0.864 | 1.364 |

512
513 The maximum values of PFA from all the floors of all the SC-MRF-CBs are lower than that of
514 the SC-MRF under the DBE. Under the FOE and MCE, all the values of PFA of the SC-MRF-
515 CBs are lower than that of the SC-MRF, with the exception of H35K167A5 and H40K133A24
516 for the FOE and MCE, respectively. The PFA reduction observed in the SC-MRF-CBs ranges

517 from 5.81% to 23.65%, from 0.73% to 17.19% and from 0.42% to 11.46%, under the FOE,
518 DBE and MCE, respectively. Thus, the new self-centering column bases can be very effective
519 in reducing the PFA of an SC-MRF that will be equipped with these column bases.

520 These results show that the SC-MRF-CBs have in general better seismic performance than the
521 SC-MRF in terms of the above two engineering demand parameters examined. Low values of
522 $\theta_{s,max}$ and PFA are associated with low non-structural and equipment damage. Thus, non-
523 structural elements and equipment installed to SC-MRF-CBs may exhibit less damage. In
524 addition, since $\theta_{s,max}$ dictates the design of columns in the serviceability limit state, there is a
525 potential of reducing the cross-sections of the members of the SC-MRF-CBs because they
526 exhibit very low values of $\theta_{s,max}$.

527 Figure 5 depicts the comparison of the height-wise distribution of $\theta_{s,max}$, of all the frames
528 studied herein under the FOE, DBE and MCE. Under the FOE, the H40K167A15,
529 H40K167A10, H40K133A24, H35K167A15, H35K167A10 and H35K200A10 have lower
530 values of $\theta_{s,max}$, for all the storeys. The rest of the SC-MRF-CBs have lower values of $\theta_{s,max}$, for
531 all the storeys, with the exception of the first storey. It is also observed that the SC-MRF-CBs
532 have lower values of $\theta_{s,max}$, for all the storeys, with the exception of the first storey under the
533 DBE level. The same trend is observed for all the frames at the MCE level, with the exception
534 of H35K200A10, H35K167A15, H35A167A10 and H40K167A15, which have lower values
535 of $\theta_{s,max}$ for all the storeys. The reason for the increased first-storey $\theta_{s,max}$ demands of most of
536 the SC-MRF-CBs is attributed to the gap openings of their self-centering column bases.

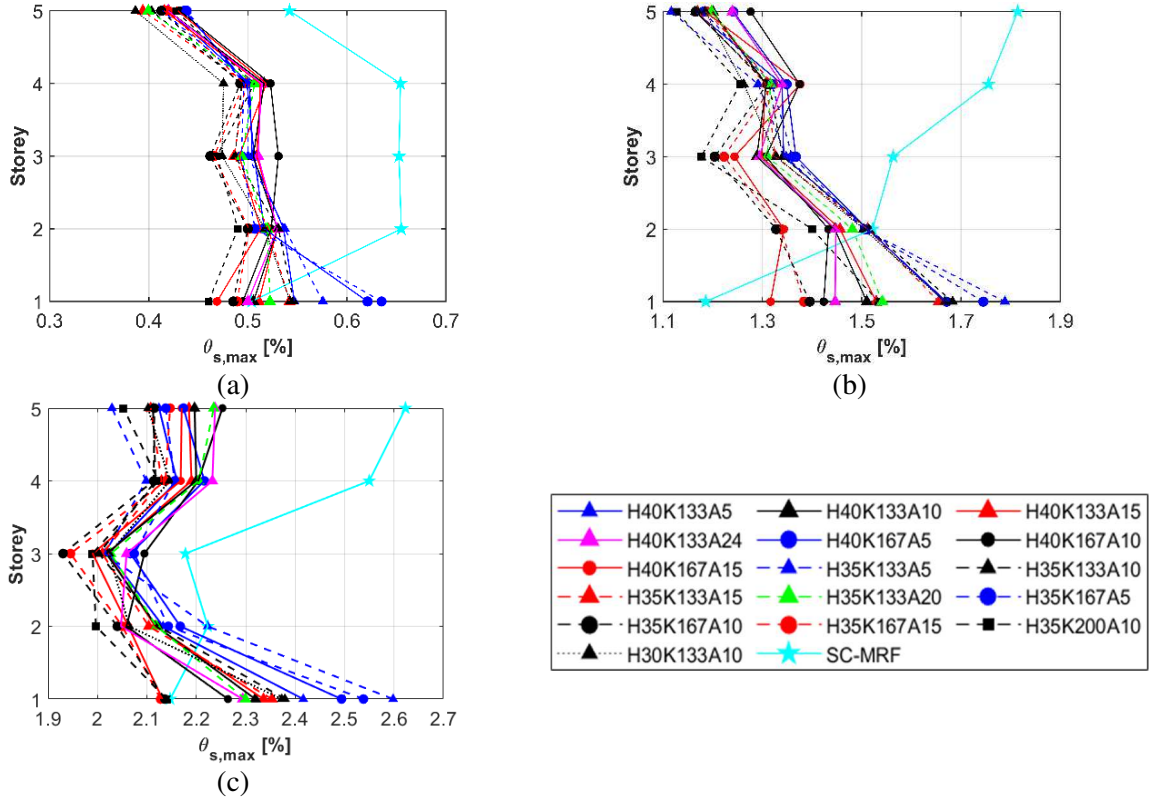
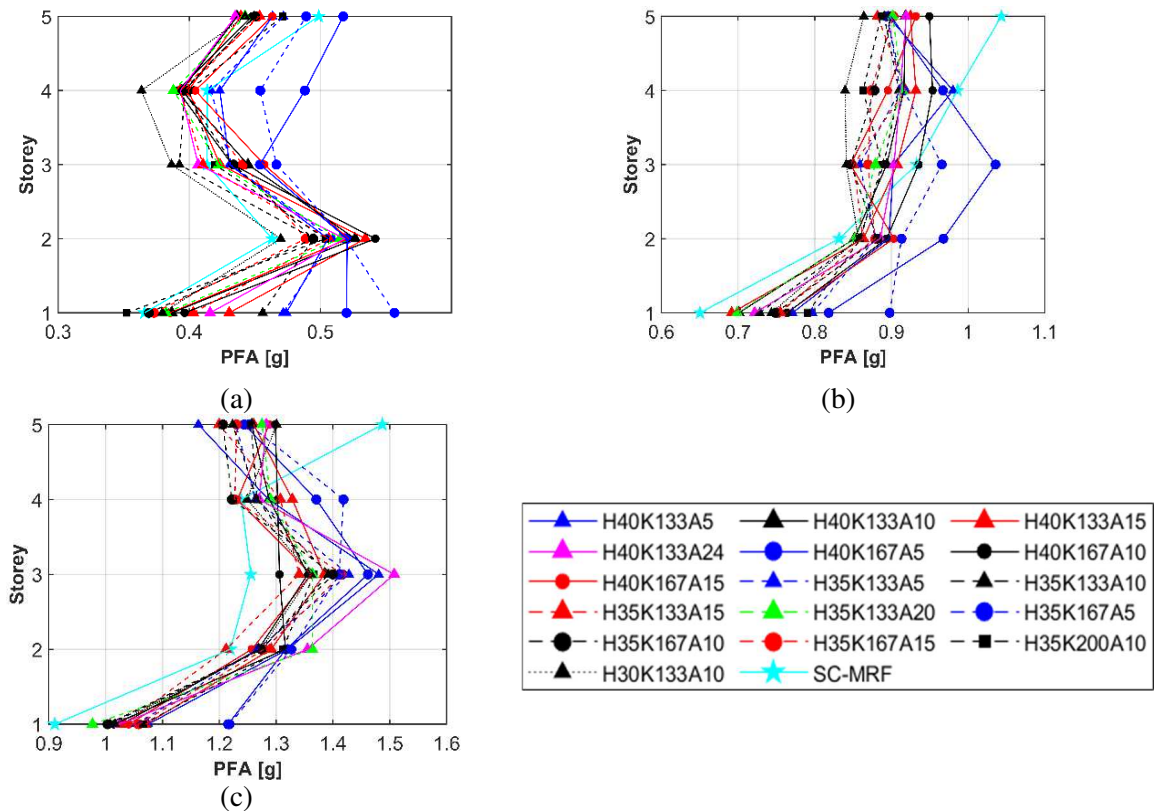


Figure 5 Comparison of the median height-wise distribution of the $\theta_{s,max}$ of the SC-MRF and SC-MRF-CB designs under the: (a) FOE; (b) DBE; and (c) MCE intensity levels.

537
538
539

540 Figure 6 shows the comparison of the height-wise distribution of PFA under the FOE, DBE
541 and MCE. Under the FOE, apart from the H35K200A10, all the other SC-MRF-CBs have
542 higher PFAs compared to that of the SC-MRF. In the second storey, all the SC-MRF-CBs have
543 higher PFAs compared to that of the SAC-MRF. In the third storey, there is a shift in this trend;
544 H30K133A10, H35K133A10, H40K133A24 and H35K133A15 have lower PFAs than that of
545 the SC-MRF. In the fourth storey, only H35K133A5, H40K133A5, H35K167A5 and
546 H40K167A5 have higher PFAs than that of the SC-MRF. Finally, in the fifth storey, apart from
547 H40K167A5, all the other SC-MRF-CBs have lower PFAs compared to that of the SC-MRF.
548 Under the DBE, the SC-MRF has PFAs lower than those of all the SC-MRF-CBs in both the
549 first and second storey. However, in the third storey, apart from H35K167A4 and H40K176A5
550 which have higher PFAs, and H40K167A10 which has similar PFA, all the other SC-MRF-
551 CBs have lower PFAs compared to that of the SC-MRF. Finally, in both the fourth and fifth
552 storeys, all the SC-MRF-CBs have lower PFAs compared to that of the SC-MRF. Under the

553 MCE, apart from H35K133A15 that has lower PFA in its second storey, all the other SC-MRF-
 554 CBs have higher PFAs in all their three first storeys as compared to those of the SC-MRF. In
 555 the fourth storey, H40K167A15, H35K167A10 and H35K167A15 have lower PFAs as
 556 compared to the SC-MRF. Lastly, in the fifth storey, all the SC-MRF-CBs have lower PFAs
 557 compared to that of the SC-MRF.



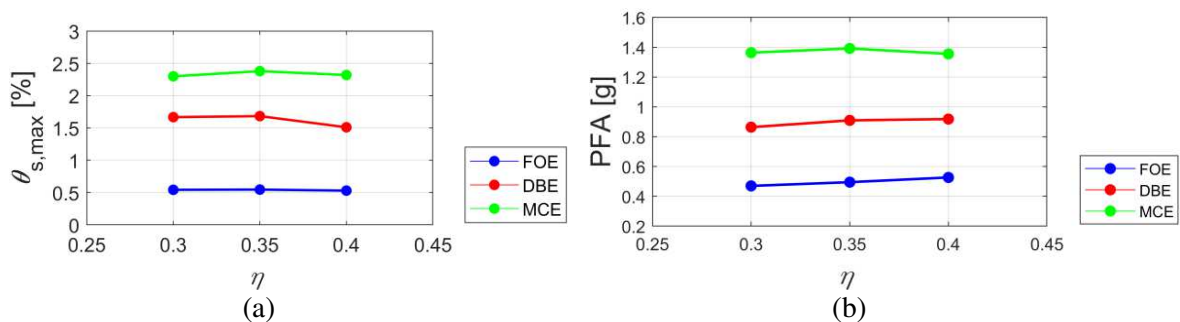
558 Figure 6 Comparison of the median height-wise distribution of the PFA of the SC-MRF and SC-
 559 MRF-CBs under the: (a) FOE; (b) DBE; and (c) MCE intensity levels.

560
 561 The PFA distribution of Figure 6 can be explained by recent studies in self-centering MRFs
 562 with connections similar to those of the SC-MRF-CBs. These suggest that the magnitudes of
 563 the PFAs and their distribution is influenced by the interactions between the beams and
 564 columns of these systems. These member interactions are due to the discontinuity of their
 565 connections and the asymmetry in member restraints due to the presence of the rocking in the
 566 column bases [61].

567 5.2 Effect of base strength and stiffness on the seismic performance of the frames

568 In this section, the effect of base strength and stiffness on the seismic performance of the frames
 569 examined herein is evaluated in terms of $\theta_{s,max}$ and PFA. The parameters η , β_{base} and α , that are
 570 associated with the base strength and stiffness of the frames, were used for this evaluation.

571 In order to evaluate the effect of base strength of the frames to the response parameters $\theta_{s,max}$
 572 and PFA, the parameter η is examined. Thus, the design cases H40K133A10, H35K133A10
 573 and H30K133A10, with η equals 0.40, 0.35 and 0.30, respectively, were compared. Figures
 574 7(a) and 7(b) show $\theta_{s,max}$ and PFA versus η , respectively, for the three seismic intensities
 575 examined. As indicated in Figure 7(a), when η increases from 0.30 to 0.35, $\theta_{s,max}$ also increases
 576 for all the seismic intensity levels. The increase observed is 0.65%, 0.93% and 3.36% under
 577 the FOE, DBE and MCE, respectively. A further increase of η to 0.40 results in a reduction of
 578 $\theta_{s,max}$ for all the seismic intensity levels. The reduction of $\theta_{s,max}$ is 2.98%, 10.27% and 2.52%
 579 under the FOE, DBE and MCE, respectively. The same trend is observed for the PFA but only
 580 for the MCE intensity level. Under FOE and DBE, an increase of η results in an increase of
 581 PFA. More specifically, when η increases from 0.30 to 0.35, PFA values increase by 5.07%
 582 and 5.02%, under the FOE and DBE, respectively. A further increase of η to 0.40 results in an
 583 increase of PFA equal to 6% and 0.94%, under the FOE and DBE, respectively.



584
 585 Figure 7 Effect of η to (a) $\theta_{s,max}$; and (b) PFA.
 586
 587

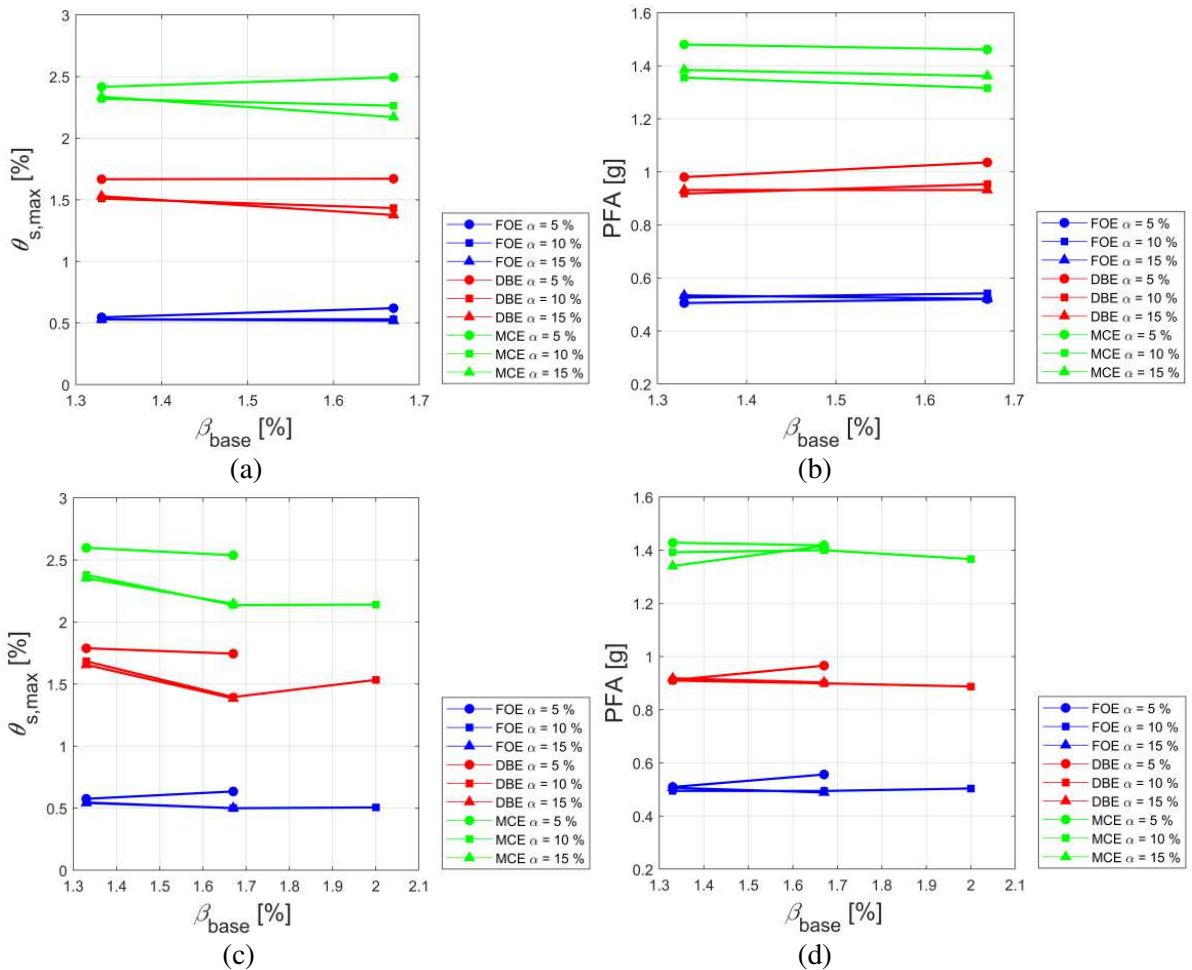
588 The design cases examined herein were compared in terms of the parameters β_{base} and α to
 589 evaluate the effect of base stiffness on their seismic response. For the frames with $\eta=0.40$, the
 590 following design cases were compared to evaluate the effect of β_{base} , i.e.: H40K133A5

591 ($\beta_{base}=133\%$) and H40K167A5 ($\beta_{base}=167\%$), which have a value of $\alpha=5\%$; H40K133A10
592 ($\beta_{base}=133\%$) and H40K167A10 ($\beta_{base}=167\%$), with $\alpha = 10\%$; and H40K133A15 ($\beta_{base}=133\%$)
593 and H40K167A15, with $\alpha=15\%$. For the frames with $\eta=0.35$, the following frames were
594 compared: H35K133A5 ($\beta_{base}=133\%$) and H35K167A5 ($\beta_{base}=167\%$), with $\alpha=5\%$;
595 H35K133A10 ($\beta_{base}=133\%$), H35K167A10 ($\beta_{base}=167\%$) and H35K200A10 ($\beta_{base}=200\%$),
596 with $\alpha=10\%$; and H35K133A15 ($\beta_{base}=133\%$) and H35K167A15 ($\beta_{base}=167\%$), with $\alpha=15\%$.
597 Figure 8 shows the effect of β_{base} to the seismic response, in terms of the $\theta_{s,max}$ and PFA, of the
598 aforementioned design cases.

599 For the frames with $\eta=0.40$ and $\alpha=5\%$, the results in Table 3 show that an increase of β_{base} from
600 133% to 167% results to higher values of $\theta_{s,max}$, for all the intensity levels. Thus, the increase
601 of $\theta_{s,max}$ observed, due to the increase of β_{base} , is 11.91%, 0.25% and 3.11%, for the FOE, DBE
602 and MCE seismic intensity levels, respectively. The same increase of β_{base} , leads to a reduction
603 of $\theta_{s,max}$ for all the seismic intensity levels for the frames with $\eta=0.40$ and $\alpha=10\%$. The
604 reduction observed equals 2.09%, 10.01% and 7.09%, under the FOE, DBE and MCE,
605 respectively. Finally, an increase of β_{base} from 133% to 167% results to lower $\theta_{s,max}$ for the
606 frames with $\eta=0.40$ and $\alpha=15\%$, under the DBE and MCE. This trend is reversed under the
607 FOE. In addition, the increase of β_{base} from 133% to 167 results to higher values of PFA under
608 the FOE and DBE, for the frames with $\eta=0.40$ and $\alpha=5\%$ and $\alpha=10\%$. In contrary, the same
609 increase of β_{base} leads to a reduction of PFA under all the seismic intensity levels for the frames
610 with $\eta=0.40$ and $\alpha=15\%$.

611 For the frames with $\eta=0.35$ and $\alpha=10\%$ and $\alpha=15\%$, results in Table 3 show that an increase of
612 β_{base} from 133% to 167% results to lower values of $\theta_{s,max}$, for all the seismic intensity levels.
613 For the frames with $\alpha=10\%$, the reduction of $\theta_{s,max}$, due to the increase of β_{base} , is 8.46%,
614 17.09% and 10.21%, under the FOE, DBE and MCE, respectively. For the frames with $\alpha=10\%$,
615 this reduction equals 7.56%, 16.40% and 8.76% under the FOE, DBE and MCE. In the frames

616 with $\eta=0.35$ and $\alpha=5\%$, an increase of β_{base} from 133% to 167% results to 2.43% and 2.31%
617 lower values of $\theta_{s,max}$, under the DBE and MCE, respectively. An opposite trend is observed
618 under the FOE. For the frames with $\eta=0.35$ and $\alpha=5\%$, results show that an increase of β_{base}
619 from 133% to 167% results to 8.46% and 5.63% higher values of PFA under the FOE and
620 DBE, respectively. Under the MCE, the PFA of the frame with $\beta_{base}=133\%$ is 0.68% larger
621 than that of with $\beta_{base}=167\%$. For the frames with $\eta=0.35$ and $\alpha=10\%$, results show that an
622 increase of β_{base} from 133% to 167% results to 0.08% and 1.14% lower values of PFA under
623 the FOE and DBE, respectively. Under the MCE, the PFA of the frame with $\beta_{base}=167\%$ is
624 0.56% larger than that of with $\beta_{base}=133\%$. A similar trend is observed for the frames with
625 $\eta=0.35$ and $\alpha=15\%$.



626
627

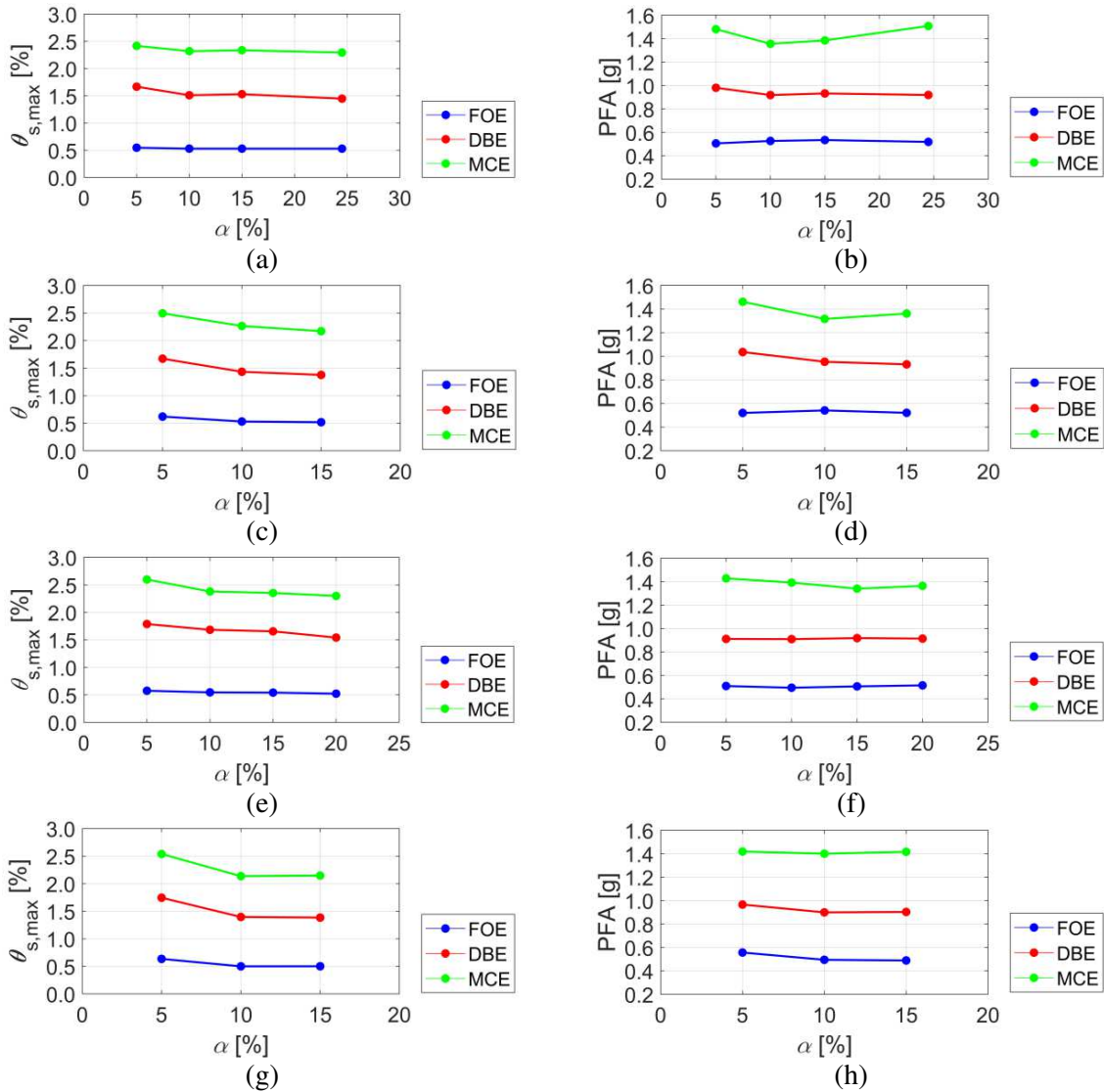
628
629
630
631
632

Figure 8 Effect of β_{base} to (a) $\theta_{s,max}$ ($\eta = 0.40$); (b) PFA ($\eta = 0.40$); (c) $\theta_{s,max}$ ($\eta = 0.35$); and (d) PFA ($\eta = 0.35$).

633 For the design cases with $\eta=0.40$, the following frames were compared to evaluate the effect
634 of α on $\theta_{s,max}$ and PFA: H40K133A5 ($\alpha=5\%$), H40K133A10 ($\alpha=10\%$), H40K133A15 ($\alpha=15\%$)
635 and H40K133A24 ($\alpha=24.5\%$), with $\beta_{base}=133\%$; and H40K167A5 ($\alpha=5\%$), H40K167A10
636 ($\alpha=10\%$) and H40K167A15 ($\alpha=15\%$), with $\beta_{base}=167\%$. This effect is shown in Figures 9(a)-
637 (d) for these design cases. It is observed that the highest value of $\theta_{s,max}$ is achieved by
638 H40K133A5 ($\alpha=5\%$) for the frames with $\beta_{base}=133\%$, under the FOE, DBE and MCE. The
639 lowest values of $\theta_{s,max}$ are achieved for the frame H40K133A24 ($\alpha=24.5\%$) for both the DBE
640 and MCE. Frame H40K133A5 with $\alpha=5\%$ has the best PFA performance, achieving the lowest
641 value of PFA under the FOE. In addition, the frame with $\alpha=10\%$ has the best PFA performance
642 under the DBE and MCE. For the frames with $\beta_{base}=167\%$, increasing the value of α from 5%
643 to 10%, results in a reduction of $\theta_{s,max}$ for all the seismic intensity levels. This reduction equals
644 14.48%, 14.22% and 9.21%, under the FOE, DBE and MCE, respectively. A further increase
645 of α from 10% to 15%, leads to a reduction of $\theta_{s,max}$, which equals 2.31%, 3.98% and 4.23%,
646 under the FOE, DBE and MCE, respectively. Increasing the value of α from 5% to 10%, leads
647 to a 3.95% increase, and 7.94% and 9.93% reduction of PFA under the FOE, DBE and MCE,
648 respectively. Finally, a further increase of α from 10% to 15%, leads to a 3.76% and 2.29%
649 reduction and 3.32% increase of PFA, under the FOE, DBE and MCE, respectively.

650 For the design cases with $\eta=0.35$, the following frames were compared: H35K133A5 ($\alpha=5\%$),
651 H35K133A10 ($\alpha=10\%$), H35K133A15 ($\alpha=15\%$) and H35K133A20 ($\alpha=20\%$), with
652 $\beta_{base}=133\%$; and H35K167A5 ($\alpha=5\%$), H35K167A10 ($\alpha=10\%$) and H35K167A15 ($\alpha=15\%$),
653 with $\beta_{base}=167\%$ (Figures 9(e)-(h)). For the frames with $\beta_{base}=133\%$, the lowest values of $\theta_{s,max}$
654 is achieved for the frame with the higher value of α , i.e., 20% (H35K133A20), for all the
655 seismic intensity levels. The frame with $\alpha=5\%$ (H35K133A10) has the best PFA performance,
656 achieving the lowest value of PFA under DBA and MCE. In addition, the frame $\alpha=15\%$ has
657 the best PFA performance under the MCE. For the frames with $\beta_{base}=167\%$, increasing the

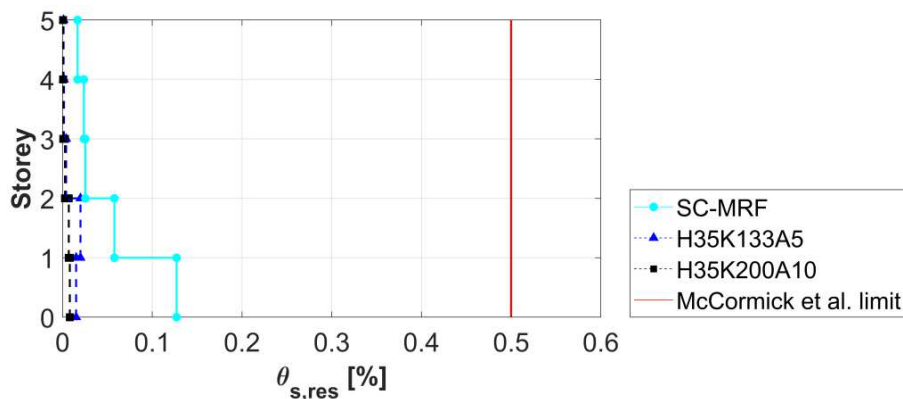
658 value of α from 5% to 10%, results in a reduction of $\theta_{s,max}$ for all the seismic intensity levels.
659 This reduction equals 21.26%, 20.02% and 15.83%, under the FOE, DBE and MCE,
660 respectively. A further increase of α from 10% to 15%, leads to a 0.23% increase, 0.83%
661 reduction and 0.49% increase of $\theta_{s,max}$, under the FOE, DBE and MCE, respectively. Increasing
662 the value of α from 5% to 10%, leads to a 11.14%, 6.89% and 1.30% reduction of PFA under
663 the FOE, DBE and MCE, respectively. Finally, a further increase of α from 10% to 15%, results
664 to a 1.14% reduction, and 0.38% and 1.14% increase of PFA, under the FOE, DBE and MCE,
665 respectively.



666 Figure 9 Effect of α to (a) $\theta_{s,max}$ ($\eta = 0.40$, $\beta_{base} = 133\%$); (b) PFA ($\eta = 0.40$, $\beta_{base} = 133\%$); (c) $\theta_{s,max}$ (η
667 = 0.40, $\beta_{base} = 167\%$); (d) PFA ($\eta = 0.40$, $\beta_{base} = 167\%$); (e) $\theta_{s,max}$ ($\eta = 0.35$, $\beta_{base} = 133\%$); (f) PFA (η
668 = 0.35, $\beta_{base} = 133\%$); (g) $\theta_{s,max}$ ($\eta = 0.35$, $\beta_{base} = 167\%$); and (h) PFA ($\eta = 0.35$, $\beta_{base} = 167\%$).
669

670 5.3 Residual drift performance of the frames

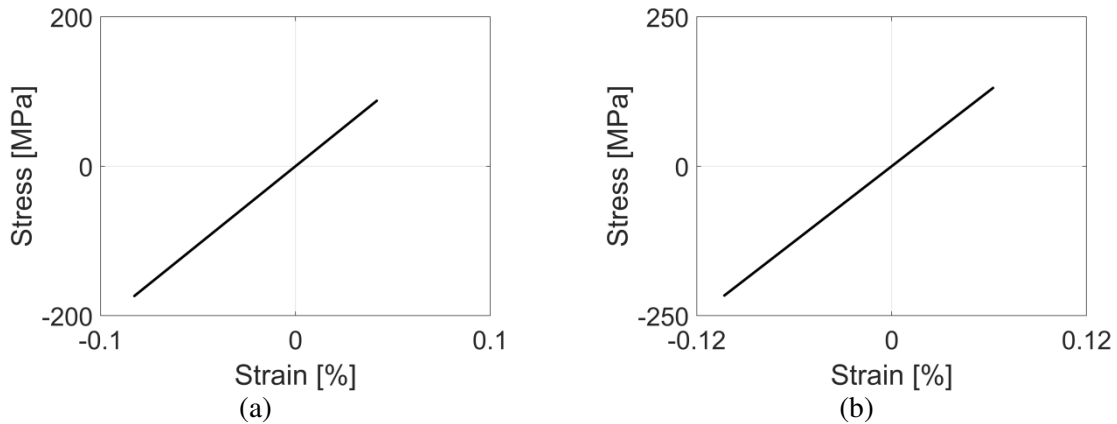
671 Figure 10 shows the height-wise distribution of the median residual drifts ($\theta_{s,res}$) of the SC-
 672 MRF, H35K133A5 and H35K200A10 under the MCE, together with a maximum allowable
 673 limit for residual drifts. This limit was proposed by McCormick et al. [62] and utilised to
 674 characterise reparability in such buildings. The rationale for presenting only these two SC-
 675 MRF-CBs is that they are those that exhibit the lowest and highest $\theta_{s,res}$ values among the
 676 investigated frames. Residual drifts are recognised as an important index of the seismic
 677 performance and resilience of structures since they are directly linked to probability of
 678 demolition of a building [34,62]. It is observed that all the frames have values of $\theta_{s,res}$ lower
 679 than the proposed limit in [62] and that both H35K133A5 and H35K200A10 have lower $\theta_{s,res}$
 680 values for all their storeys than those of the SC-MRF. These values are almost negligible.



681 Figure 10 Height-wise distribution of median residual drifts of the SC-MRF, H35K133A5 and
 682 H35K200A10 under the MCE, plotted against the maximum allowable limit for residual interstorey
 683 drifts proposed by McCormick et al. [62].

684
 685 Figure 11 shows the stress-strain hysteresis loops in the flanges of the first-storey columns
 686 (Figure 3(a)) of the H35K133A5 and H35K200A10 under the 1992 Landers earthquake scaled
 687 to the MCE. It is observed, that the two SC-MRF-CBs do not exhibit any plastic deformation
 688 in their first-storey columns since the developed maximum stress at the extreme fibers of their
 689 flanges is well below the yield stress limit of 355 MPa. Thus, damage is avoided at their self-
 690 centering column bases. This shows that the values of $\theta_{s,res}$ observed in SC-MRF-CBs (Figure
 691 10) mainly result from permanent deformations that occur at PT beam-column connections.

692 Similar results are observed for the rest of the SC-MRF-CBs and ground motions but are not
 693 shown herein due to lack of space.



694 Figure 11 Stress strain hysteresis loops of a flange of a first storey column of: (a) H35K133A5; and
 695 (b) H35K200A10 under the 1992 Landers earthquake scaled to MCE.
 696

697

6 COLLAPSE ASSESSMENT

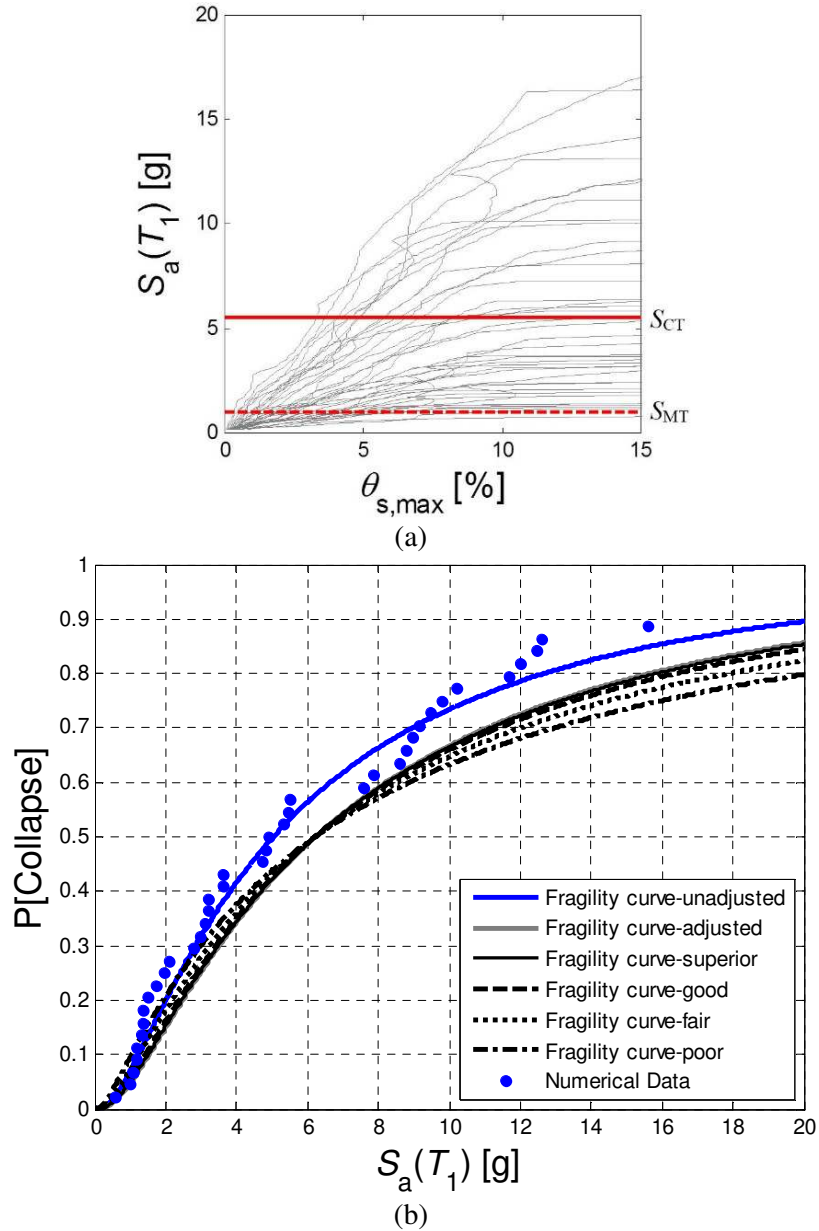
698 The collapse resistance of the frames is determined by the use of IDA [63]. $S_a(T_1)$ is the IM
 699 used herein and $\theta_{s,max}$ was the response parameter monitored. The set of ground motions used
 700 for the non-linear dynamic analyses in Section 5 were used also for the IDAs. For each design
 701 case and ground motion, the collapse $S_a(T_1)$ value at which $\theta_{s,max}$ increases without bound was
 702 obtained. To determine the limit of collapse, the criterion adopted by Seo et al. [64] was used.
 703 Thus, the incremental slopes were calculated by drawing straight lines between the consecutive
 704 data points in the IDA curve. The lowest $S_a(T_1)$ value corresponding to the i^{th} data point with
 705 the slope between the i^{th} and $i+1^{th}$ points being less than 10% of the initial slope on the IDA
 706 curve was defined as the collapse $S_a(T_1)$. The initial slope was determined from the straight line
 707 from the origin of axis to the first data point of the IDA curve. A collapse fragility curve was
 708 generated by fitting a lognormal cumulative distribution function to the collapse $S_a(T_1)$ values
 709 determined for each frame. The median value, S_{CT} , and the lognormal standard deviation, β , of
 710 collapse $S_a(T_1)$ values define this distribution. The value of S_{CT} was amplified to take into
 711 account the effect of the distinct spectral shape of rare ground motions, characterised by the
 712 parameter ε [65]. In this work, the simplified methodology proposed by FEMA P695 [59] is

713 adopted, where the influence of the spectral shape is taken into account by the use of a spectral
714 shape factor (*SSF*). Thus, the values of S_{CT} of all the frames of this study were multiplied by
715 *SSF* to estimate their true collapse capacity.

716 The parameter β affects the shape of the fragility curve and is a measure of the level of
717 uncertainty in the analysis results. The system-level and the record-to-record uncertainty were
718 used for the construction of the fragility curves. The FEMA P695 [59] regulations were used
719 for the calculation of the total uncertainty, where additional system-level uncertainty were
720 added from three categories [43]. The total uncertainty of the system, β_{Total} , is given by:

$$721 \quad \beta_{Total} = \sqrt{\beta_{RTR}^2 + \beta_{DR}^2 + \beta_{TD}^2 + \beta_{MDL}^2} \quad (13)$$

722 where β_{RTR} is the record-to-record uncertainty, β_{DR} , β_{TD} and β_{MDL} are the additional uncertainty
723 because of the robustness of the design requirements, the accuracy of the test data and the
724 accuracy of the numerical model, respectively. The values of β_{RTR} were taken from the results
725 of the IDA, while values of the rest uncertainties were based on P695 recommendations [59].
726 Thus, the uncertainties β_{DR} , β_{TD} and β_{MDL} can be subjectively classified as ‘superior’, ‘good’,
727 ‘fair’, or ‘poor’ [59]. The uncertainty due to the robustness of the design requirements, accuracy
728 of the test data and numerical model were assigned each rating of ‘superior’, ‘good’, ‘fair’ and
729 ‘poor’ together to construct four different collapse fragility curves. The values of uncertainty
730 for ‘superior’, ‘good’, ‘fair’ and ‘poor’ uncertainty rating were 0.1, 0.2, 0.35 and 0.5,
731 respectively. Figure 12 shows the IDA curves of the H35K200A10 together with the collapse
732 fragility curves, for different uncertainty ratings as per the aforementioned procedure.



733 Figure 12 (a) IDA curves; and (b) corresponding collapse fragility curves of the H35K200A10.

734

735 Finally, the constructed collapse fragility curves were used for the evaluation of the collapse

736 risk of the frames through the adjusted collapse margin ratio ($ACMR$), defined as:

737
$$ACMR = \frac{S_{CT}}{S_{MT}} \cdot SSF \quad (14)$$

738 where S_{CT} , is the median collapse intensity of the frames and S_{MT} is the intensity demand to the

739 MCE-level intensity.

740 **7 EFFECT OF BASE STRENGTH AND STIFFNESS ON THE COLLAPSE RISK OF**
 741 **THE FRAMES**

742 Table 4 shows the collapse capacity results of all the investigated frames. The SC-MRF-CBs
 743 have larger value of collapse capacity and *ACMR*, compared to the SC-MRF. The maximum
 744 increase in collapse capacity and *ACMR* is achieved by the H35K200A10 compared to SC-
 745 MRF, whereas the minimum increase of these parameters is achieved by the H35K133A5.
 746 Collapse capacity and *ACMR* of the SC-MRF-CBs design cases are 25.08-33.23% and 23.02-
 747 27.95% higher, respectively, than that of the SC-MRF. Thus, there is a significant improvement
 748 of the collapse capacity and *ACMR*, by adopting the self-centering column bases and
 749 appropriately tuning their base stiffness and strength characteristics.

750 Figure 13 shows the collapse fragility curves of the SC-MRF, H35K133A5 and H35K200A10
 751 for different uncertainty ratings. These two SC-MRF-CBs were selected because they achieve
 752 the lower and higher increase of *ACMR*, compared to the SC-MRF. It is observed that the
 753 H35K133A5 and H35K200A10 are exhibiting, in general, the lowest probabilities of collapse.
 754 This trend is inverted for low values of $S_a(T_1)$, for superior, good and fair uncertainty ratings,
 755 and for poor uncertainty ratings the probabilities of collapse are similar for all the frames.

756

Table 4. Collapse capacity results.

| Frame | S_{MT} (g) | S_{CT} (g) | <i>CMR</i> | <i>SSF</i> | <i>ACMR</i> |
|------------|--------------|--------------|------------|------------|-------------|
| SC-MRF | 0.90 | 3.70 | 4.10 | 1.23 | 5.06 |
| H40K133A5 | 0.93 | 5.04 | 5.44 | 1.23 | 6.72 |
| H40K133A15 | 0.93 | 5.17 | 5.57 | 1.23 | 6.88 |
| H40K167A15 | 0.95 | 5.39 | 5.67 | 1.23 | 6.97 |
| H40K167A5 | 0.95 | 5.28 | 5.56 | 1.23 | 6.83 |
| H40K133A10 | 0.93 | 5.19 | 5.60 | 1.23 | 6.92 |
| H40K167A10 | 0.95 | 5.38 | 5.66 | 1.23 | 6.95 |
| H40K133A24 | 0.92 | 5.04 | 5.45 | 1.24 | 6.74 |
| H35K133A5 | 0.93 | 4.94 | 5.32 | 1.23 | 6.57 |
| H35K133A15 | 0.93 | 5.18 | 5.59 | 1.23 | 6.87 |
| H35K167A15 | 0.95 | 5.32 | 5.60 | 1.23 | 6.89 |
| H35K167A5 | 0.95 | 5.27 | 5.54 | 1.23 | 6.80 |
| H35K133A10 | 0.93 | 5.19 | 5.60 | 1.23 | 6.91 |
| H35K167A10 | 0.95 | 5.35 | 5.64 | 1.23 | 6.92 |

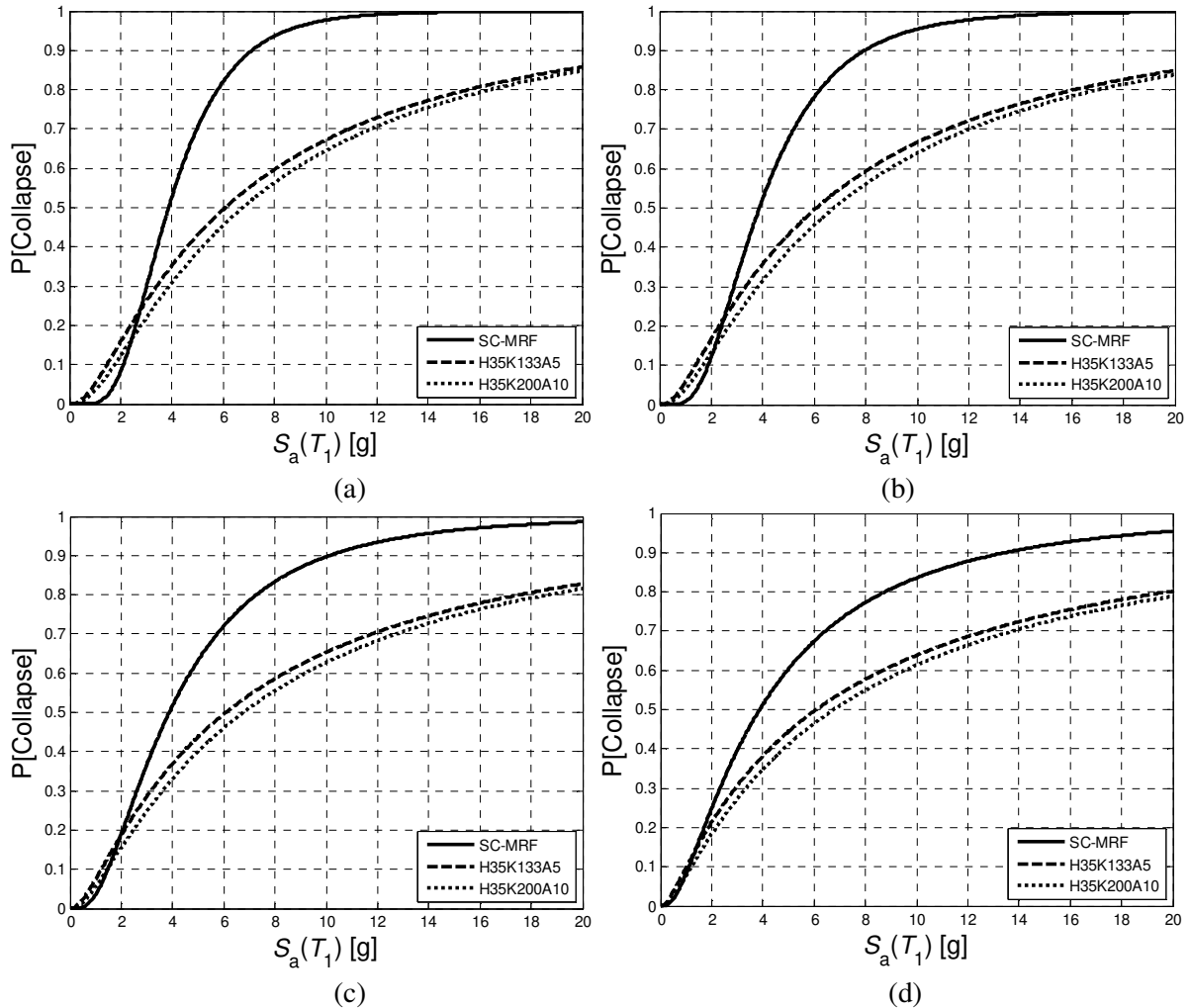
| | | | | | |
|------------|------|------|------|------|------|
| H35K200A10 | 0.97 | 5.54 | 5.74 | 1.22 | 7.02 |
| H35K133A20 | 0.93 | 5.04 | 5.43 | 1.23 | 6.70 |
| H30K133A10 | 0.93 | 5.11 | 5.51 | 1.23 | 6.81 |

757
758 To evaluate the effect of base strength on the collapse risk of the frames, the base strength
759 factor η was utilised. To this end, the design cases H40K133A10, H35K133A10 and
760 H30K133A10, with η equals 0.40, 0.35 and 0.30, respectively, were compared. The
761 H40K133A10 has the largest value of *ACMR* among the frames compared, indicating that the
762 frame with the largest value of η has the lowest collapse risk. When the value of η is increased
763 from 0.30 to 0.35, the *ACMR* is increased by 1.5%. In addition, the value of *ACMR* for the
764 H40K133A10 with $\eta = 0.40$ is 1.61% higher than that of the H30K133A10 with $\eta = 0.30$. Thus,
765 the collapse risk of the frames is reduced for higher values of η .

766 The frames examined here were compared in terms of their base factors β_{base} and α to assess
767 the effect of base stiffness on their collapse risk. For the frames with $\eta=0.40$, the following
768 frames were compared to evaluate the effect of β_{base} , i.e.: H40K133A5 ($\beta_{base}=133\%$) and
769 H40K167A5 ($\beta_{base}=167\%$), which have a value of $\alpha=5\%$; H40K133A10 ($\beta_{base}=133\%$) and
770 H40K167A10 ($\beta_{base}=167\%$), with $\alpha=10\%$; and H40K133A15 ($\beta_{base}=133\%$) and H40K167A15,
771 with $\alpha=15\%$. For the frames with $\eta=0.35$, the following frames were compared: H35K133A5
772 ($\beta_{base}=133\%$) and H35K167A5 ($\beta_{base}=167\%$), with $\alpha=5\%$; H35K133A10 ($\beta_{base}=133\%$),
773 H35K167A10 ($\beta_{base}=167\%$) and H35K200A10 ($\beta_{base}=200\%$), with $\alpha=10\%$; and H35K133A15
774 ($\beta_{base}=133\%$) and H35K167A15 ($\beta_{base}=167\%$), with $\alpha=15\%$.

775 The results in Table 4 indicate that an increase of β_{base} from 133% to 167% results to higher
776 values of *ACMR* for the frames with $\eta=0.40$. Thus, the increase of *ACMR* observed, due to the
777 increase of β_{base} , is 1.63%, 0.46% and 1.21% for the design cases with α equals 5%, 10% and
778 15%, respectively. Similar results are obtained for the frames with $\eta=0.35$. The values of
779 *ACMR* of the frames with β_{base} equal to 167% are 3.40%, 0.12% and 0.29% higher than those
780 of the frames with β_{base} equal to 133%, when α equals 5%, 10% and 15%, respectively. In

781 addition, the frame H35K200A10 ($\beta_{base}=200\%$) has 1.46% and 1.58% higher values of $ACMR$
 782 than those of the H35K167A10 ($\beta_{base}=167\%$) and H35K133A10 ($\beta_{base}=133\%$), respectively.
 783 Thus, it can be concluded that the collapse resistance of the frames is increased for frames with
 784 higher values of β_{base} , representing the initial base stiffness.



787
788
789 Figure 13 Collapse fragility curves of SC-MRF, H35K133A5 and H35K200A10 for: (a) superior; (b)
790 good; (c) fair; and (d) poor uncertainty rating.

791
792 For the design cases with $\eta=0.40$, the following frames were compared to evaluate the effect
793 of α : H40K133A5 ($\alpha=5\%$), H40K133A10 ($\alpha=10\%$), H40K133A15 ($\alpha=15\%$) and
794 H40K133A24 ($\alpha=24.5\%$), with $\beta_{base}=133\%$; and H40K167A5 ($\alpha=5\%$), H40K167A10
795 ($\alpha=10\%$) and H40K167A15 ($\alpha=15\%$), with $\beta_{base}=167\%$. The results indicate that the higher
796 value of $ACMR$ is achieved by H40K133A10 ($\alpha=10\%$), for the frames with $\beta_{base}=133\%$. Thus,
797 collapse resistance of the frames is increased by 2.89% when α increases from 5% to 10%, and

798 is then reduced for further increase of α . For the frames with $\beta_{base}=167\%$ a different trend is
799 observed, with *ACMR* having higher values when α increases. Thus, the frame H40K167A15
800 ($\alpha=15\%$) has 0.22% and 1.96% higher values of *ACMR* than those of H40K167A10 ($\alpha=10\%$)
801 and H40K167A5 ($\alpha=5\%$), respectively.

802 For the design cases with $\eta=0.35$ the following frames were compared: H35K133A5 ($\alpha=5\%$),
803 H35K133A10 ($\alpha=10\%$), H35K133A15 ($\alpha=15\%$), and H35K133A20 ($\alpha=20\%$), with
804 $\beta_{base}=133\%$; and H35K167A5 ($\alpha=5\%$), H35K167A10 ($\alpha=10\%$) and H35K167A15 ($\alpha=15\%$),
805 with $\beta_{base}=167\%$. The results of the frames with $\beta_{base}=133\%$ demonstrate that the *ACMR* is
806 increased when α is increased from 5% to 15% and is then reduced for further increase of α . A
807 similar trend is observed for the frames with $\beta_{base}=167\%$.

808 **8 CONCLUSIONS**

809 The potential of the SC-MRF-CBs to improve the seismic performance and reduce the collapse
810 risk of earthquake-resilient steel buildings with SC-MRFs was examined. The effect of strength
811 and stiffness characteristics of the novel self-centering column base to improve the seismic
812 performance and collapse capacity of the SC-MRF-CBs was also investigated. The parameters
813 through which these effects were taken into consideration were three normalised factors that
814 represent the initial stiffness, post-yield stiffness and strength of the self-centering column
815 bases. These structural properties of the self-centering column bases can be independently
816 adjusted by utilising the analytical expressions that are presented in this research, thereby
817 changing also the initial stiffness, post-yield stiffness and strength of the whole SC-MRF-CBs.
818 A step-by-step design procedure for the self-centering column bases, which is enhanced
819 compared to that in [29], is also proposed to that purpose. The evaluation of the seismic
820 performance and collapse risk of the SC-MRF-CBs was based on a prototype steel building
821 designed to incorporate different seismic-resistant frames, i.e., one SC-MRF and sixteen SC-
822 MRF-CBs' designs with different base stiffness and strength characteristics. A set of 44 ground

823 motions that were scaled to three seismic intensity levels was utilised to perform non-linear
824 dynamic analyses and evaluate the seismic performance of the frames. Moreover, IDA was
825 used with the same set of ground motions to evaluate the collapse capacity of the frames.
826 Finally, fragility curves and the *ACMR* of the frames were derived to compare their seismic
827 risk.

828 On the basis of the findings of this paper, the following conclusions can be drawn:

- 829 1. The SC-MRF-CBs have in general better seismic performance than the SC-MRF in
830 terms of $\theta_{s,max}$ and PFA. The results demonstrate that the self-centering column base is
831 very effective in reducing $\theta_{s,max}$ and PFA, by only tuning its base stiffness and strength
832 characteristics. Thus, non-structural elements and equipment installed to SC-MRF-CBs
833 will potentially exhibit less damage. A potential of reducing the cross-sections of the
834 members of the SC-MRF-CBs can be also concluded. That is because the SC-MRF-
835 CBs exhibit $\theta_{s,max}$ values lower than the relevant limits of EC8 under the FOE, DBE
836 and MCE. This reduction reaches an appreciable 24.05%.
- 837 2. The H35K133A5 and H35K200A10 (i.e., the two frames that exhibit the lowest and
838 highest values of $\theta_{s,res}$ among the investigated SC-MRF-CBs) have lower values of $\theta_{s,res}$
839 in all their storeys, compared to those of the SC-MRF. These values are almost
840 negligible and are solely due to permanent deformations in the PT beam-column
841 connections since the self-centering column bases behave elastically up to their targeted
842 rotations.
- 843 3. The SC-MRF-CBs have superior collapse capacity compared to the SC-MRF. The
844 collapse capacity and *ACMR* of the SC-MRF-CBs are increased by up to 33.23% and
845 27.95%, respectively, compared to the SC-MRF.
- 846 4. The collapse risk of the SC-MRF-CBs is reduced for higher values of η . The
847 H40K133A10, with $\eta=0.40$, has the largest value of *ACMR* and, thus, the lowest

848 collapse risk compared to the frames with η equal to 0.35 and 0.30, all having the same
849 initial and post-yield stiffness.

850 5. It is concluded that collapse capacity of the frames is increased for frames with higher
851 values of β_{base} . The SC-MRF-CBs with $\beta_{base}=167\%$ have superior collapse resistance
852 than the ones with $\beta_{base}=133\%$, when $\eta=0.40$. The maximum increase of *ACMR*
853 observed, due to the increase of β_{base} , is 1.63% for the design cases with $\alpha=5\%$. Similar
854 results are obtained for the frames with $\eta=0.35$. The values of *ACMR* of the frames with
855 $\beta_{base}=167\%$ are 3.40%, 0.12% and 0.29% higher than those of the frames with
856 $\beta_{base}=133\%$, when α equals 5%, 10% and 15%, respectively. In addition, the frame
857 H35K200A10 ($\beta_{base}=200\%$) has 1.46% and 1.58% higher values of *ACMR* than those
858 of the H35K167A10 ($\beta_{base}=167\%$) and H35K133A10 ($\beta_{base}=133\%$), respectively.

859 6. The results for the SC-MRF-CBs with $\eta=0.40$ indicate that the higher value of *ACMR*
860 is achieved by the frame with $\alpha=10\%$, for the frames with $\beta_{base}=133\%$. Thus, the
861 collapse capacity of the frames increases by 2.89% when α increases from 5% to 10%
862 and is then reduced for further increase of α . For the frames with $\beta_{base}=167\%$, a different
863 trend is observed, with *ACMR* having higher values when α is increased up to 15%.

864 7. For the SC-MRF-CBs with $\eta=0.35$ and $\beta_{base}=133\%$, it is observed that the *ACMR* is
865 increased when α is increased from 5% to 15% and is then reduced for further increase
866 of α . A similar trend is observed for the frames with $\beta_{base}=167\%$. Thus, an increase of
867 α up to a certain value leads to an increase of the collapse capacity of the frames. It is
868 also concluded that α is more effective in increasing the collapse capacity of the frames
869 compared to β_{base} , because a similar increase of the collapse capacity is achieved by
870 increasing both parameters, but for a larger increase of β_{base} .

871 8. It is concluded that the best seismic performance and highest collapse capacity among
872 the SC-MRF-CBs examined is achieved for a combination of the strength factor, η ,

873 equal to 0.35; initial stiffness factor, β_{base} , equal to 200%; and post-yield stiffness ratio,
874 α , equal to 10%.

875 REFERENCES

- 876 [1] H. Inamasu, D.G. Lignos, A.M. Kanvinde, Effect of column base flexibility on the
877 hysteretic response of wide flange steel columns, 3rd Huixian Int. Forum Earthq. Eng.
878 Young Res. August 11-12. (2017) Paper No. 260.
879 https://infoscience.epfl.ch/record/230104/files/260_Inamasu_Hiroyuki_fullpaper.pdf.
- 880 [2] F. Zareian, A. Kanvinde, Effect of column-base flexibility on the seismic response and
881 safety of steel moment-resisting frames, *Earthq. Spectra*. 29 (2013) 1537–1559.
882 doi:10.1193/030512EQS062M.
- 883 [3] J. Ruiz-García, A. Kanvinde, Effect of column base flexibility on residual drift demands
884 of low-rise steel moment-resisting frames, in: 2013 World Congr. Adv. Struct. Eng. Eng.
885 Mech. (ASEM13), Sept. 8-12, Jeju, Korea, 2013: pp. 627–639.
- 886 [4] P.A. Torres-Rodas, F. Flores, F. Zareian, Seismic response of steel moment frame
887 considering gravity system and column base flexibility, in: Proc. 11th US Natl. Conf.
888 Earthq. Eng., June 25-29, Los Angeles, USA, 2018.
889 [https://www.researchgate.net/profile/Pablo_Torres-](https://www.researchgate.net/profile/Pablo_Torres-Rodas/publication/327663389_Seismic_Response_of_Steel_Moment_Frames_considering_gravity_system_and_column_base_flexibility/links/5b9c618292851ca9ed0aa655/Seismic-Response-of-Steel-Moment-Frames-considering)
890 [Rodas/publication/327663389_Seismic_Response_of_Steel_Moment_Frames_considering_gravity_system_and_column_base_flexibility/links/5b9c618292851ca9ed0aa655/Seismic-Response-of-Steel-Moment-Frames-considering](https://www.researchgate.net/profile/Pablo_Torres-Rodas/publication/327663389_Seismic_Response_of_Steel_Moment_Frames_considering_gravity_system_and_column_base_flexibility/links/5b9c618292851ca9ed0aa655/Seismic-Response-of-Steel-Moment-Frames-considering).
- 893 [5] A. Aviram, B. Stojadinovic, A. Der Kiureghian, Performance and reliability of exposed
894 column base plate connections for steel moment-resisting frames, Berkeley, CA, USA,
895 2010.
- 896 [6] BS EN 1998-1, Eurocode 8: Design of structures for earthquake resistance - Part 1:
897 General rules, seismic actions and rules for buildings., 2013.
- 898 [7] P.T. Rodas, F. Zareian, A. Kanvinde, Hysteretic Model for Exposed Column–Base
899 Connections, *J. Struct. Eng.* (2016) 04016137. doi:10.1061/(ASCE)ST.1943-
900 541X.0001602.
- 901 [8] D.G. Lignos, H. Krawinkler, A database in support of modeling of component
902 deterioration for collapse prediction of steel frame structures, in: John W. Wallace (Ed.),
903 *Struct. Eng. Res. Front.* May 16-19, Long Beach, California, United States, 2007: pp.
904 1–12. doi:doi: 10.1061/40944(249)31.
- 905 [9] H.-J. Kim, C. Christopoulos, Seismic design procedure and seismic response of post-
906 tensioned self-centering steel frames, *Earthquake Eng. Struct. Dyn.* 38 (2009) 355–376.
907 doi:10.1002/eqe.859.
- 908 [10] A.S. Tzimas, A.I. Dimopoulos, T.L. Karavasilis, EC8-based seismic design and
909 assessment of self-centering steel frames with viscous dampers, *J. Constr. Steel Res.* 105
910 (2015) 60–73.
- 911 [11] J.M. Ricles, R. Sause, M.E.M. Garlock, C. Zhao, Posttensioned seismic-resistant
912 connections for steel frames, *J. Struct. Eng.* 127 (2001) 113–121.
- 913 [12] K.-C. Tsai, C.-C. Chou, C.-L. Lin, P.-C. Chen, S.-J. Jhang, Seismic self-centering steel
914 beam-to-column moment connections using bolted friction devices, *Earthq. Eng. Struct.*
915 *Dyn.* 37 (2008) 627–645. doi:10.1002/eqe.779.
- 916 [13] G. Vasdravellis, T.L. Karavasilis, B. Uy, Large-scale experimental validation of steel
917 post-tensioned connections with web hourglass pins, *J. Struct. Eng.* 139 (2013) 1033–
918 42. doi:10.1061/(ASCE)ST.1943-541X.0000696.
- 919 [14] G. Vasdravellis, T.L. Karavasilis, B. Uy, Design rules, experimental evaluation, and

- 920 fracture models for high-strength and stainless-steel hourglass shape energy dissipation
 921 devices, *J. Struct. Eng.* 140 (2014) 04014087. doi:10.1061/(ASCE)ST.1943-
 922 541X.0001014.
- 923 [15] P. Rojas, J.M. Ricles, R. Sause, Seismic Performance of Post-tensioned Steel Moment
 924 Resisting Frames with Friction Devices, *J. Struct. Eng.* 131 (2005) 529–540.
 925 doi:10.1061/(ASCE)0733-9445(2005)131:4(529).
- 926 [16] C.-C. Chou, Y.-C. Wang, J.-H. Chen, Seismic design and behavior of post-tensioned
 927 steel connections including effects of a composite slab, *Eng. Struct.* 30 (2008) 3014–
 928 3023. doi:10.1016/j.engstruct.2008.04.013.
- 929 [17] M.A. Chowdhury, A. Rahmzadeh, M.S. Alam, Improving the seismic performance of
 930 post-tensioned self-centering connections using SMA angles or end plates with SMA
 931 bolts, *Smart Mater. Struct.* 28 (2019) 075044.
- 932 [18] M.A. Chowdhury, A. Rahmzadeh, S. Moradi, M.S. Alam, Feasibility of using reduced
 933 length superelastic shape memory alloy strands in post-tensioned steel beam–column
 934 connections, *J. Intell. Mater. Syst. Struct.* 30 (2018) 283–307.
 935 doi:10.1177/1045389X18806393.
- 936 [19] B. Uy, Innovative connections for the demountability and rehabilitation of steel, space
 937 and composite structures, in: 12th Int. Conf. Steel, Sp. Compos. Struct. 28-30 May,
 938 Prague, Czech Republic, 2014: pp. 99–109.
- 939 [20] J. Liu, Design for Deconstruction with Demountable Composite Beams and Floor
 940 Systems, *Eng. J.* 53 (2016) 107–16.
- 941 [21] S. Pampanin, C. Christopoulos, M.J.N. Priestley, Performance-based seismic response
 942 of frame structures including residual deformations. Part II: Multi-degree of freedom
 943 systems., *J. Earthq. Eng.* 7 (2003) 119–147.
- 944 [22] C. Christopoulos, A. Filiatrault, B. Folz, Seismic response of self-centring hysteretic
 945 SDOF systems, *Earthq. Eng. Struct. Dyn.* 31 (2002) 1131–1150. doi:10.1002/eqe.152.
- 946 [23] C. Christopoulos, Frequency Response of Flag-Shaped Single Degree-of-Freedom
 947 Hysteretic Systems, *J. Eng. Mech.* 130 (2004) 894–903. doi:10.1061/(ASCE)0733-
 948 9399(2004)130:8(894).
- 949 [24] C. Christopoulos, S. Pampanin, M.J.N. Priestley, Performance-based seismic response
 950 of frame structures including residual deformations. Part 1: Single-degree of freedom
 951 systems., *J. Earthq. Eng.* 7 (2003) 97–118.
- 952 [25] T.L. Karavasilis, C.-Y. Seo, Seismic structural and non-structural performance
 953 evaluation of highly damped self-centering and conventional systems, *Eng. Struct.* 33
 954 (2011) 2248–2258. doi:10.1016/j.engstruct.2011.04.001.
- 955 [26] G.P. Cimellaro, Simultaneous stiffness–damping optimization of structures with respect
 956 to acceleration, displacement and base shear, *Eng. Struct.* 29 (2007) 2853–2870.
 957 doi:10.1016/j.engstruct.2007.01.001.
- 958 [27] C.-C. Chou, J.-H. Chen, Analytical model validation and influence of column bases for
 959 seismic responses of steel post-tensioned self-centering MRF systems, *Eng. Struct.* 33
 960 (2011) 2628–2643. doi:10.1016/j.engstruct.2011.05.011.
- 961 [28] BS EN 1998-3, Eurocode 8 : Design of structures for earthquake resistance — Part 3:
 962 Assessment and retrofitting of buildings., 2005.
- 963 [29] V.C. Kamperidis, T.L. Karavasilis, G. Vasdravellis, Self-centering steel column base
 964 with metallic energy dissipation devices, *J. Constr. Steel Res.* 149 (2018) 14–30.
 965 doi:10.1016/j.jcsr.2018.06.027.
- 966 [30] H. Chi, J. Liu, Seismic behavior of post-tensioned column base for steel self-centering
 967 moment resisting frame, *J. Constr. Steel Res.* 78 (2012) 117–130.
 968 doi:10.1016/j.jcsr.2012.07.005.
- 969 [31] X.-T. Wang, C.-D. Xie, L.-H. Lin, J. Li, Seismic behavior of self-centering concrete-

- 970 filled square steel tubular (CFST) Column Base, *J. Constr. Steel Res.* 156 (2019) 75–85.
 971 doi:<https://doi.org/10.1016/j.jcsr.2019.01.025>.
- 972 [32] M. Latour, G. Rizzano, A. Santiago, L. Simões da Silva, Experimental response of a
 973 low-yielding, self-centering, rocking column base joint with friction dampers, *Soil Dyn.*
 974 *Earthq. Eng.* 116 (2019) 580–592. doi:<https://doi.org/10.1016/j.soildyn.2018.10.011>.
- 975 [33] B. Wang, S. Zhu, C.-X. Qiu, H. Jin, High-performance self-centering steel columns with
 976 shape memory alloy bolts: Design procedure and experimental evaluation, *Eng. Struct.*
 977 182 (2019) 446–458. doi:<https://doi.org/10.1016/j.engstruct.2018.12.077>.
- 978 [34] FEMA, FEMA P-58-1 Seismic performance assessment of buildings - Volume 1 -
 979 Methodology (2nd Edition), Washington, DC, USA, 2018.
 980 <https://www.fema.gov/media-library/assets/documents/90380>.
- 981 [35] A.S. Tzimas, G.S. Kamaris, T.L. Karavasilis, C. Galasso, Collapse risk and residual drift
 982 performance of steel buildings using post-tensioned MRFs and viscous dampers in near-
 983 fault regions, *Bull. Earthq. Eng.* 14 (2016) 1643–1662. doi:10.1007/s10518-016-9898-
 984 3.
- 985 [36] A.I. Dimopoulos, T.L. Karavasilis, G. Vasdravellis, B. Uy, Seismic design, modelling
 986 and assessment of self-centering steel frames using post-tensioned connections with web
 987 hourglass shape pins, *Bull. Earthq. Eng.* 11 (2013) 1797–1816. doi:10.1007/s10518-
 988 013-9437-4.
- 989 [37] ASTM, ASTM A416/A416M-05, Standard Specification for Steel Strand, Uncoated
 990 Seven-Wire for Prestressed Concrete, West Conshohocken, PA, USA, 2005.
- 991 [38] T.L. Bruce, M.R. Eatherton, Behavior of Post-Tensioning Strand Systems Subjected to
 992 Inelastic Cyclic Loading, *J. Struct. Eng.* 142 (2016) 04016067.
 993 doi:10.1061/(ASCE)ST.1943-541X.0001503.
- 994 [39] P. Sideris, A.J. Aref, A. Filiatrault, Effects of anchorage hardware on the cyclic tensile
 995 response of unbonded monostrands, *PCI J.* 59 (2014) 60–77.
 996 doi:10.15554/pcij.06012014.60.77.
- 997 [40] G.A. MacRae, C.R. Urmson, W.R. Walpole, P. Moss, K. Hyde, C. Clifton, Axial
 998 shortening of steel columns in buildings subjected to earthquakes, *Bull. New Zeal. Soc.*
 999 *Earthq. Eng.* 42 (2009) 275–287.
- 1000 [41] R. Vargas, M. Bruneau, Analytical Response and Design of Buildings with Metallic
 1001 Structural Fuses. I, *J. Struct. Eng.* 135 (2009) 386–93. doi:10.1061/(ASCE)0733-
 1002 9445(2009)135:4(386).
- 1003 [42] Y.-C. Lin, R. Sause, J.M. Ricles, Seismic Performance of a Large-Scale Steel Self-
 1004 Centering Moment-Resisting Frame: MCE Hybrid Simulations and Quasi-Static
 1005 Pushover Tests, *J. Struct. Eng.* 139 (2013) 1227–1236. doi:10.1061/(ASCE)ST.1943-
 1006 541X.0000661.
- 1007 [43] T.C. Steele, L.D.A. Wiebe, Collapse risk of controlled rocking steel braced frames with
 1008 different post-tensioning and energy dissipation designs, *Earthq. Eng. Struct. Dyn.*
 1009 (2017). doi:10.1002/eqe.2892.
- 1010 [44] BS EN 1993-1-1, Eurocode 3: Design of steel structures - Part 1-1: General rules and
 1011 rules for steel buildings, United Kingdom, 2009.
- 1012 [45] BS EN 1993-1-8, Eurocode 3 : Design of steel structures — Part 1-8 : Design of joints,
 1013 United Kingdom, 2010.
- 1014 [46] L. Wiebe, C. Christopoulos, Performance-Based Seismic Design of Controlled Rocking
 1015 Steel Braced Frames. I: Methodological Framework and Design of Base Rocking Joint,
 1016 *J. Struct. Eng.* 141 (2015). doi:10.1061/(ASCE)ST.1943-541X.0001202.
- 1017 [47] G. Vasdravellis, T.L. Karavasilis, B. Uy, Finite element models and cyclic behavior of
 1018 self-centering steel post-tensioned connections with web hourglass pins, *Eng. Struct.* 52
 1019 (2013) 1–16. doi:<http://dx.doi.org/10.1016/j.engstruct.2013.02.005>.

- 1020 [48] U. of C. Pacific Earthquake Engineering Research Center (PEER), OpenSees, (2015).
1021 <http://opensees.berkeley.edu>.
- 1022 [49] M.H. Scott, G.L. Fenves, Plastic hinge integration methods for force-based beam-
1023 column elements, *J. Struct. Eng.* 132 (2006) 244–252.
- 1024 [50] D.G. Lignos, H. Krawinkler, Deterioration Modeling of Steel Components in Support
1025 of Collapse Prediction of Steel Moment Frames under Earthquake Loading, *J. Struct.*
1026 *Eng.* 137 (2011) 1291–1302. doi:10.1061/(ASCE)ST.1943-541X.0000376.
- 1027 [51] M. Hamidia, A. Filiatrault, A.J. Aref, Simplified seismic sidesway collapse analysis of
1028 frame buildings, *Earthq. Eng. Struct. Dyn.* 43 (2014) 429–448. doi:10.1002/eqe.2353.
- 1029 [52] H. Krawinkler, Shear in Beam-Column Joints in Seismic Design of Frames, *Eng. J.* 15
1030 (1978).
- 1031 [53] C.C. Chou, K.C. Tsai, W.C. Yang, Self-centering steel connections with steel bars and
1032 a discontinuous composite slab, *Earthq. Eng. Struct. Dyn.* 38 (2009) 403–422.
1033 doi:10.1002/eqe.856.
- 1034 [54] G. Vasdravellis, M. Banguera, D. Al-Sammarai, Robustness assessment of a steel self-
1035 centering moment-resisting frame under column loss, *J. Constr. Steel Res.* 141 (2018)
1036 36–49. doi:10.1016/j.jcsr.2017.11.004.
- 1037 [55] M. Bruneau, C.-M. Uang, R. Sabelli, Ductile design of steel structures, Second Edi,
1038 McGraw-Hill Education, 2011.
- 1039 [56] P. Uriz, Towards Earthquake Resistant Design of Concentrically Braced Steel
1040 Structures, University of California, Berkeley, USA, 2005.
- 1041 [57] VSL International Ltd, Post-tensioning, stay cables & construction methods, Prod.
1042 Broch. VSL STRAND POST-TENSIONING Syst. (2013). www.vsl.com.
- 1043 [58] M. Banguera, G. Vasdravellis, T.L. Karavasilis, Ultralow Cycle Fatigue Tests and
1044 Fracture Prediction Models for Duplex Stainless-Steel Devices of High Seismic
1045 Performance Braced Frames, *J. Struct. Eng.* 145 (2019) 04018230. doi:10.1061/(ASCE)
1046 ST.1943-541X.0002243.
- 1047 [59] FEMA, Quantification of building seismic performance factors (FEMA P695) (ATC-63
1048 Project), USA, 2009. https://www.fema.gov/media-library-data/20130726-1716-25045-9655/fema_p695.pdf.
- 1050 [60] ASCE/SEI, Seismic rehabilitation of existing buildings (ASCE/SEI 41-06), U.S.A.,
1051 2007.
- 1052 [61] L.T. Kibriya, C. Málaga-Chuquitaypea, M.M. Kashani, N.A. Alexander, Nonlinear
1053 dynamics of self-centring rocking steel frames using finite element models, *Soil Dyn.*
1054 *Earthq. Eng.* 1115 (2018) 826–37. doi:<https://doi.org/10.1016/j.soildyn.2018.09.036>.
- 1055 [62] J. McCormick, H. Aburano, M. Ikenaga, M. Nakashima, Permissible Residual
1056 Deformation Levels for Building Structures Considering both Safety and Human
1057 Elements, in: 14th World Conf. Earthq. Eng. Oct. 12-17, China Earthquake
1058 Administration Ministry of Construction, Beijing, China, 2008.
- 1059 [63] D. Vamvatsikos, C.A. Cornell, Incremental dynamic analysis, *Earthq. Eng. Struct. Dyn.*
1060 31 (2002) 491–514. doi:10.1002/eqe.141.
- 1061 [64] C.Y. Seo, T.L. Karavasilis, J.M. Ricles, R. Sause, Seismic performance and probabilistic
1062 collapse resistance assessment of steel moment resisting frames with fluid viscous
1063 dampers, *Earthq. Eng. Struct. Dyn.* 43 (2014) 2059–2216. doi:10.1002/eqe.2440.
- 1064 [65] J.W. Baker, C.A. Cornell, Spectral shape, epsilon and record selection, *Earthq. Eng.*
1065 *Struct. Dyn.* 35 (2006) 1077–95. doi:10.1002/eqe.571.
- 1066